A. Kuzmin, X-ray absorption spectroscopy in high-entropy material research,
in *High-Entropy Alloys: Design, Manufacturing, and Emerging Applications*,
G. Yasin, M. Abubaker Khan, M. Afifi, T. Anh Nguyen, Y. Zhang (Eds.), pp. 121-155 (Elsevier, 2024).

Doi: 10.1016/B978-0-443-22142-2.00006-5.

6 – X-ray absorption spectroscopy in high-entropy material research

Alexei Kuzmin

Institute of Solid State Physics, University of Latvia, Riga, Latvia

---

Abstract

This chapter introduces the use of X-ray absorption spectroscopy (XAS) in studying the local electronic and atomic structure of high-entropy materials. The element selectivity of XAS makes it particularly suitable to address the challenges posed by the study of multicomponent compounds. By analysing different parts of the X-ray absorption spectra for each element, one can obtain information on its chemical state from the X-ray absorption near-edge structure (XANES) and its local environment, distortions, and lattice dynamics from the extended X-ray absorption fine structure (EXAFS). The theoretical background underlying X-ray absorption spectra and existing data analysis procedures are briefly described, with particular emphasis on advanced atomistic modelling techniques that enable more reliable extraction of structural information. Finally, an overview of the applications of the XAS technique in studying high-entropy materials is presented.

Keywords: X-ray Absorption Spectroscopy; XAS; Extended X-ray Absorption Fine Structure; EXAFS; X-ray Absorption Near-Edge Structure; XANES; X-ray Absorption Fine Structure; XAFS; Reverse Monte Carlo; RMC; Multiple-Scattering; MS; Fourier Transform; FT; High-Entropy Material; HEM; High-Entropy Alloy; HEA; High-Entropy Oxide; HEO

Preprint submitted to Elsevier *November 12, 2024*

6.1. Introduction

High-entropy materials (HEMs) are a class of materials that contain five or more principal elements in equal or near-equal atomic fraction (Brechtl & Liaw (2021); George et al. (2019)). The first HEMs were high-entropy alloys (HEAs) or multicomponent alloys, discovered in the early 2000s (Yeh et al. (2004); Cantor et al. (2004)). The entropy engineering concepts were later extended to many other materials (Lei et al. (2019)), including oxides (Rost et al. (2015); Sarkar et al. (2018); Albedwawi et al. (2021); Xiang et al. (2021)), chalcogenides (Fan et al. (2016); Wei et al. (2020); Cavin et al. (2021); Chen et al. (2022); Buckingham et al. (2022); Nemani et al. (2023)), hydroxides (Teplonogova et al. (2022); Kim et al. (2022); Ritter et al. (2022)), metal-organic frameworks (Ma et al. (2021); Hu et al. (2021); Yuan et al. (2022)), and polymers (Qian et al. (2021); Huang et al. (2021)). One of the key features of HEMs is their high configurational entropy, which arises from the mixing of multiple elements (Brechtl & Liaw (2021); George et al. (2019)) and favors the formation of a compositionally and site disordered atomic structure (Miracle & Senkov (2017); Zhang et al. (2022b)). At the same time, the local atomic structure in HEMs can exhibit a certain degree of clustering or chemical short-range ordering (SRO), which depends strongly on their composition. The local coordination environment around each element is determined by its size, charge, and electronegativity, as well as the presence of other elements. The bond lengths between atoms depend on the types of atoms involved, as well as their relative positions in the structure. Therefore understanding of the local atomic structure of HEMs and how it is related to their chemical composition and properties is essential for designing and optimizing these materials for various applications.

X-ray absorption spectroscopy (XAS) is a well-established experimental method that provides information on the local electronic and atomic structure of a particular element in a material. The method is complementary to X-ray diffraction and is especially suitable for investigating local lattice distortions or the local environment around impurities with concentrations down to the ppm level, in crystalline, nanocrystalline and disordered materials. XAS is well-adapted to the study of multicomponent compounds because of its element selectivity, which is achieved by tuning the photon energy in the X-ray absorption edge region of the desired element. Samples in different aggregate states, such as solids, liquids, and gases, can be probed equally well under a wide range of external conditions, including temperature, pressure, external magnetic or electric fields, as well as in oxidising or reducing environments. Suitable solid samples can be prepared in the form of single crystals, powders, thin films or nanoparticles. Samples of metals or alloys can be used either in the form of foil or as a single piece. Time-dependent X-ray absorption experiments are possible using fast scanning techniques, special experimental setups (such as dispersive ones), or pulsed X-ray sources (such as X-ray free electron lasers).

Recent advances in XAS are related to the progress and availability of synchrotron radiation sources, which ensure high-quality experimental data and open up new possibilities for time-dependent and extreme condition studies. In addition, laboratory XAS spectrometers using different X-ray tubes as a source of X-rays are also available today and are becoming increasingly popular. While they cannot compete with synchrotron radiation sources in terms of intensity and various other parameters, their daily availability and relative affordability make X-ray tubes attractive for such applications as prescreening of samples, industrial use, and user training.

6.2. Basics of X-ray Absorption Spectroscopy

X-ray photons with energies sufficient to excite an electron from the core level (1s, 2s or 2p) in an atom are usually employed in XAS when one is interested in the structural information. However, the upper levels (3s, 3p, 3d, ...) can be also used in the case of transition metals and more heavy elements to probe the local electronic structure.

The X-ray absorption spectra are designated following to the absorption edges as K, L, M, etc., which are classified according to the electron principal quantum number n values of 1, 2, 3, respectively. In the X-ray absorption spectra, the electric-dipole-induced transitions play the most important role, so that the electric dipole selection rules apply for the orbital angular momentum $\Delta l = \pm 1$. For example, the K-edge X-ray absorption spectrum corresponds to transitions from $1s_{1/2}$ level to empty np states, L_1-edge from $2s_{1/2}$ level to empty np states, L_2-edge from $2p_{1/2}$ level to empty $nd_{3/2}$ states, and L_3-edge from $2p_{3/2}$ level to empty $nd_{3/2}$ and $nd_{5/2}$ states. The transitions from the 2p levels to ns states are also allowed but have weak intensity and, therefore, are usually neglected.

The electron excited by an X-ray photon is often called the photoelectron. The minimum (threshold) energy E_0 required to eject the photoelectron is equal to the electron binding energy. Therefore, the wavenumber k of the photoelectron is related to the incident X-ray photon energy E and to the threshold energy E_0 as $k = \sqrt{(2m_e/\hbar^2)(E - E_0)}$, where m_e is the electron mass, and $\hbar$ is Plank's constant.

When a core-shell electron is excited by an X-ray photon, the absorbing atom goes to an excited state with a positively charged core hole (inner shell vacancy) located at the electron initial core level. The excitation lifetime Δt can be estimated from Heisenberg's uncertainty principle $\Delta E \Delta t \sim \hbar/2$, where ΔE is the core shell natural width, and is equal to about 10^{-15}-10^{-16} seconds. Note that this time is much smaller than the characteristic time of thermal vibrations equal to 10^{-13}-10^{-14} seconds, so that the absorbing and surrounding atoms remain frozen on their positions during the photoabsorption process. At the same time, the presence of the core hole leads to a relaxation of other (passive) electrons in the absorbing atom. Finally, the return of an excited atom to the ground state occurs through various relaxation channels. Light elements with small atomic numbers Z relax mainly nonradiatively via the production of Auger electrons, whereas relaxation of heavy elements is mostly radiative via the emission of X-ray fluorescence (XRF) photons.

When monochromatic X-rays with an energy E travel through a homogeneous sample of thickness x, they are absorbed in a material so that their incident $I_0(E)$ and the transmitted $I(E)$ intensities are given by the Beer-Lambert law:

$$I(E) = I_0(E) e^{-\mu(E)x} \tag{1}$$

where $\mu(E)$ is the linear X-ray absorption coefficient.

The experimental measurements of the X-ray absorption coefficient $\mu(E)$ can be performed in transmission mode or using indirect detection modes, such as XRF mode, Auger electron yield and total electron yield (TEY) modes, and X-ray excited optical luminescence (XEOL) mode (Fig. 1). The fluorescence detection is advantageous for dilute samples and heavy elements. The Auger and TEY modes are suitable for light elements and surface limited (depths up to about 100 Å) studies. XEOL mode provides site-selective information on the local structure of luminescent centres.

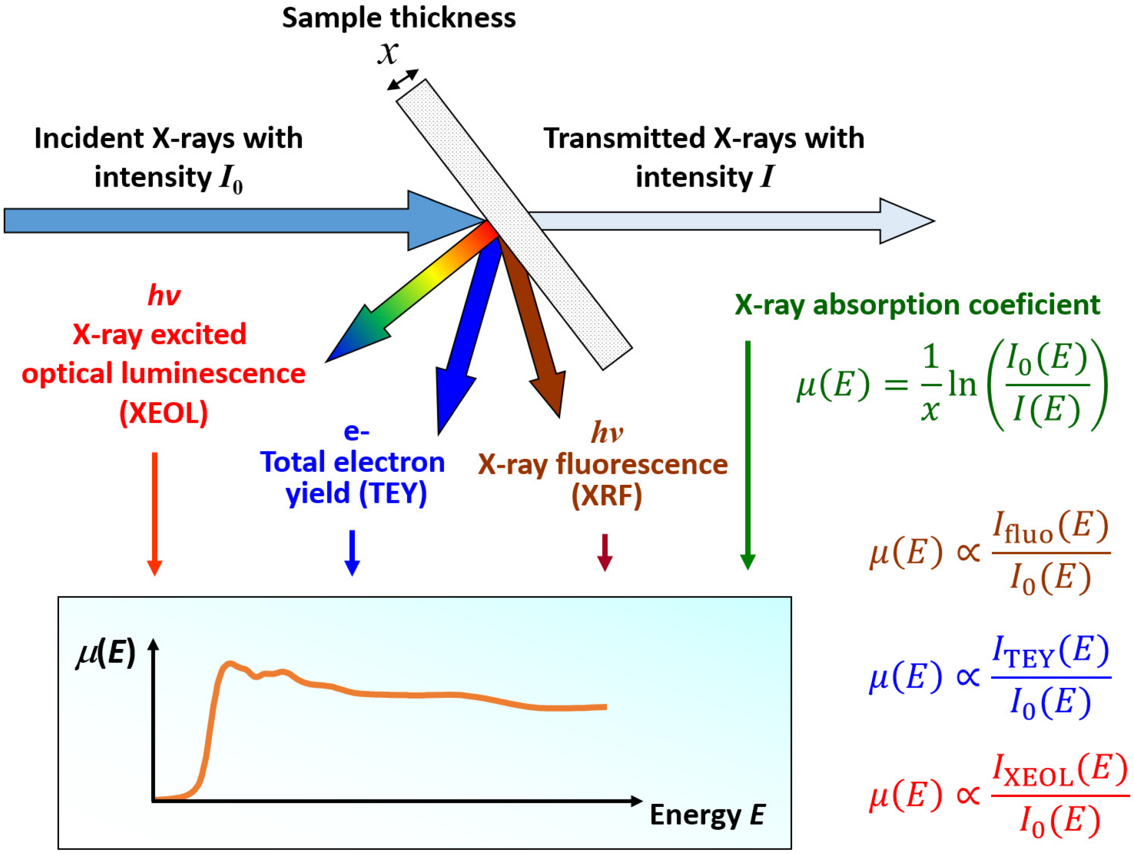

Figure 1: Four different detection modes of X-ray absorption spectrum. X-ray absorption experiment in transmission, XRF, TEY, and XEOL modes. *TEY*, Total electron yield; *XEOL*, X-ray-excited optical luminescence; *XRF*, X-ray fluorescence.

The X-ray absorption coefficient $\mu(E)$ in the one-electron approximation is proportional to the transition rate between the initial core-state i and the final excited-state f of an electron, which is given by Fermi's Golden rule:

$$\mu(E) \propto \sum_f \left| \langle f|\hat{H}|i\rangle \right|^2 \delta(E_f - E_i - E) \tag{2}$$

where $E = \hbar\omega$ is the X-ray photon energy, and the transition operator $\hat{H} = \hat{\epsilon} \cdot \vec{r}$ in the dipole approximation. Note that the final state of the electron is the relaxed excited state in the presence of the core-hole screened by other electrons.

It is common to divide the X-ray absorption spectrum into two parts: X-ray absorption near edge structure (XANES), located near the absorption edge, and extended X-ray absorption fine structure (EXAFS), which extends far beyond the edge. Though the two parts have the same physical origin, their distinction is convenient for the interpretation. The XANES region (typically within 30-50 eV of the absorption edge) contains information on the local electronic structure and is sensitive to the oxidation state of the absorbing atom, the type and distribution of empty electron states, the local symmetry and multi-electron effects. The EXAFS part contains information on the local atomic structure, including pair and many-atom distribution functions. Its analysis can provide structural information such as the coordination numbers, interatomic distances and their variations due to static and thermal disorder.

The oscillating part of the absorption coefficient, that is, EXAFS, $\chi^l(E)$ (Fig. 2) located above the absorption edge of orbital type l is defined as

$$\chi^l(k) = \frac{\mu(E) - \mu_0(E) - \mu_b(E)}{\mu_0(E)} \tag{3}$$

where $\mu_b(E)$ is the background absorption, and $\mu_0(E)$ is the atomic-like absorption due to an isolated absorbing atom (Lee et al. (1981)). It is common to display the EXAFS spectrum as a function of the wavenumber k, often multiplied by k^n (where $n = 1, 2, 3$) (Fig. 3(a)). The contributions of different coordination shells to the EXAFS spectrum can be visualized in the R-space by calculating the direct Fourier transform (FT) (Fig. 3(b)). The peaks in FT can be observed up to certain values of R, which correlate with half of the mean-free path (MFP) of the photoelectron. However, the presence of static and/or thermal disorder can significantly reduce contributions from the distant coordination shells in the FT.

It is important to note that while the shape of the Fourier transform may appear similar to that of the radial distribution function (RDF), there is a fundamental difference between these two functions. The positions of peaks in the FT are always shifted to shorter distances compared to their crystallographic values due to the presence of the phase shift in the EXAFS equation, and the shape of peaks in the FT is distorted due to the presence of the scattering amplitude. Furthermore, the FT also includes the contributions from high-order distribution functions, known as multiple-scattering (MS) effects (Natoli et al. (1990); Rehr & Albers (2000)).

The theoretical description of EXAFS in the framework of the MS theory (Rehr & Albers

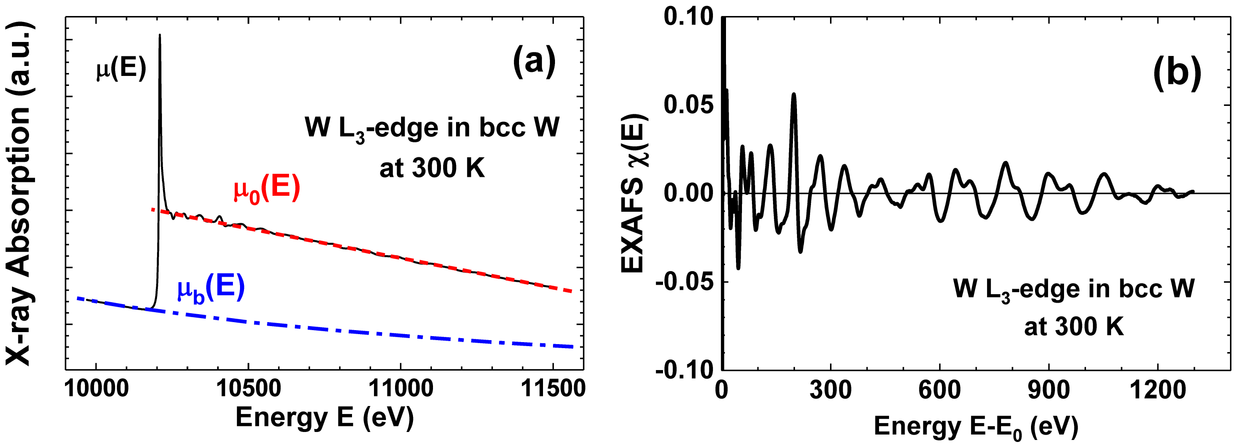

Figure 2: Extraction of the EXAFS from the X-ray absorption coefficient. The W L$_3$-edge X-ray absorption spectrum $\mu(E)$ (a) and extracted W L$_3$-edge EXAFS $\chi(E)$ (b) of BCC tungsten at 300 K. Background $\mu_b(E)$ and atomic $\mu_0(E)$ contributions are shown in (a). *BCC*, body-centered cubic; *EXAFS*, extended X-ray absorption fine structure.

(2000); Rehr et al. (2009)) is given using a series:

$$\begin{aligned} \chi^l(k) &= \sum_{n=2}^{\infty} \chi_n^l(k), \\ \chi_n^l(k) &= \sum_j A_n^l(k, R_j) \sin[2kR_j + \phi_n^l(k, R_j)] \end{aligned} \qquad (4)$$

which includes contributions $\chi_n^l(k)$ from the $(n-1)$th-order scattering processes of the excited photoelectron by the neighbouring atoms, before it returns to the absorbing atom (Rehr & Albers (2000); Ruiz-Lopez et al. (1988)). The fast convergence of the MS series occurs at least at high-k values due to the finite lifetime of the excitation, the scattering path lengths, interference cancellation effects, and path disorder. In practice, the MS contributions up to the eight-order can be calculated, for example, using *ab initio* FEFF code (Ankudinov et al. (1998); Rehr et al. (2010)).

An alternative description of the EXAFS $\chi^l(k)$ in terms of the nth-order distribution functions $g_n(R)$ is also known:

$$\begin{aligned} \chi^l(k) &= \int 4\pi R^2 \rho_0 g_2(R)[\chi_2^{oio}(k) + \chi_4^{oioio}(k) + \ldots]dR \\ &+ \iiint 8\pi^2 R_1^2 R_2^2 \sin(\theta) \rho_0^2 g_3(R_1, R_2, \theta) \\ &\times [2\chi_3^{oijo}(k) + 2\chi_4^{oiojo}(k) + \chi_4^{oijio}(k) + \chi_4^{ojijo}(k) + \ldots]dR_1 dR_2 d\theta \end{aligned}$$

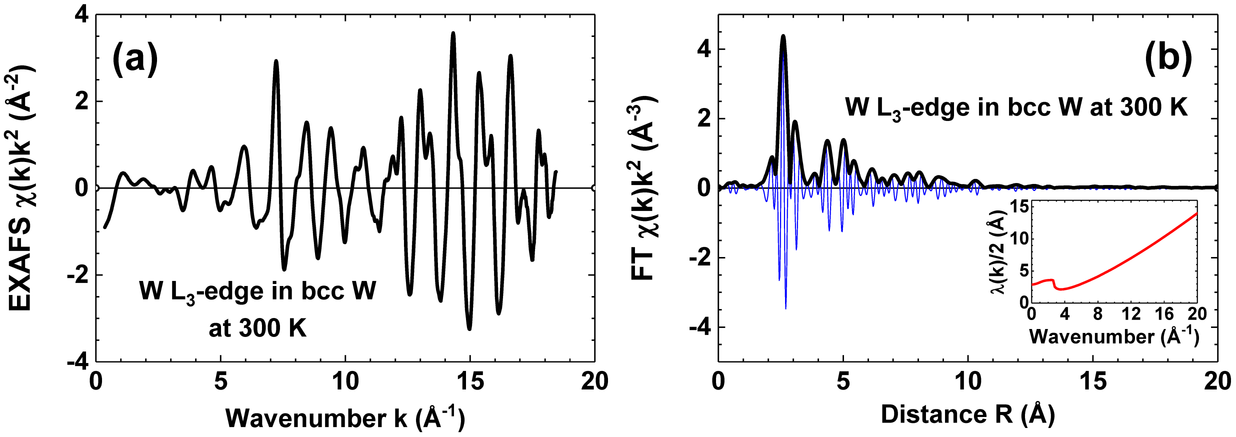

Figure 3: The W L$_3$-edge EXAFS spectrum and its FT for BCC tungsten at 300 K. The W L$_3$-edge EXAFS spectrum $\chi(k)k^2$ (a) and its Fourier transform (b) for BCC tungsten at 300 K. Both the modulus (*thick line*) and imaginary (*thin line*) parts are shown (b). The inset in (b) shows the calculated mean free path $\lambda(k)$ of a photoelectron, including the core–hole effect, plotted versus wavenumber k for the W L$_3$-edge. *BCC*, Body-centered cubic; *EXAFS*, extended X-ray absorption fine structure; *FT*, Fourier transform.

$$\begin{aligned} &+ \iiiint\!\!\int 8\pi^2 R_1^2 R_2^2 R_3^2 \sin[\theta] \rho_0^3 g_4(R_1, R_2, \theta, R_3, \Omega) \\ &\times [2\chi_4^{oijko}(k) + 2\chi_4^{oikjo}(k) + 2\chi_4^{ojiko}(k) + \ldots] dR_1 dR_2 d\theta dR_3 d\Omega \\ &+ \ldots \end{aligned} \qquad (5)$$

where ρ_0 is the average density of a system, and $\chi_m(k)$ are the MS EXAFS contributions of the $(m-1)$ order generated within a group of atoms (o, i, j, ...) described by g_n (Filipponi et al. (1995); Filipponi & Di Cicco (1995)). This approach was implemented in the GNXAS code (Di Cicco (1995); Filipponi & Di Cicco (2000)), which is able to account for the two-body (g_2), three-body (g_3), and four-body (g_4) distribution functions.

Note that there is a relation between the MS contributions χ_m and many-body distribution functions g_n (Fig. 4). Each function g_n accounts for all scattering processes involving the respective group of n-atoms, whereas each MS contribution χ_m accounts for the MS processes of the $(m-1)$th-order involving all possible atomic configurations.

6.3. Multicomponent extended X-ray absorption fine structure analysis

The analytical expression for EXAFS can be greatly simplified when one needs to extract information only from the first coordination shell of the absorbing atom.

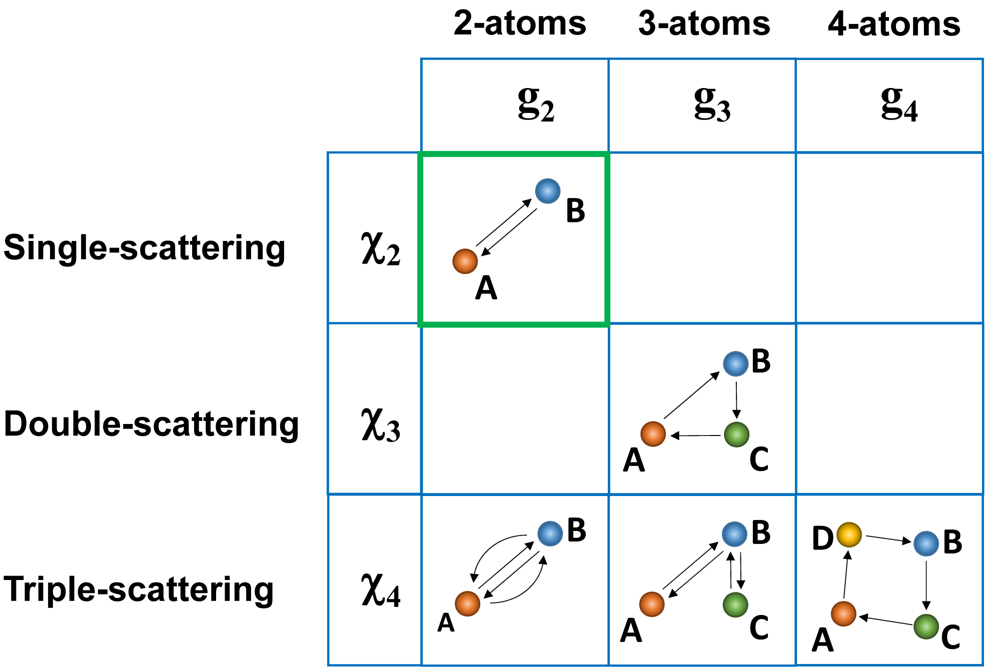

Figure 4: The relation between the scattering paths due to the multiple-scattering contributions χ_n and many-body distribution functions g_n. The scattering paths involving two atoms (A and B), tree atoms (A–C), and three atoms (A–D) are shown. χ_2 corresponds to the SS contribution for a pair of atoms A and B. χ_3 represents the double-scattering contribution generated within a group of three atoms A–C. χ_4 includes three triple-scattering contributions generated within three groups of two (A and B), three (A–C), and four (A–D) atoms. *SS*, Single-scattering.

The contribution of the first coordination shell to the total EXAFS spectrum can be isolated by the Fourier filtering procedure and analysed within the single-scattering approximation, since the lengths of all MS paths are longer than the first coordination shell radius. Thus only the first term of the series given by Eq. (4) remains. In the case of a Gaussian distribution (or in the harmonic approximation), the EXAFS expression takes a simple form

$$\begin{aligned} \chi_2^l(k) &= S_0^2 \sum_i N_i \frac{|f_{\text{eff}}^l(k,R_i)|}{kR_i^2} \exp\left[-\frac{2R_i}{\lambda(k)}\right] \\ &\times \sin[2kR_i + \phi^l(k,R_i)] \exp(-2\sigma_i^2 k^2) \end{aligned} \tag{6}$$

where S_0^2 is the amplitude reduction factor (typically between 0.8 and 1.0); N_i is the coordination number; R_i is the interatomic distance; $\lambda(k)$ is the photoelectron MFP; $f_{\text{eff}}^l(k,R)$ and $\phi^l(k,R)$ are the photoelectron effective scattering amplitude and phase shift functions; $\sigma^2(T) = \sigma_{st}^2 + \sigma_{th}^2(T)$ is the Debye-Waller (DW) factor or mean-squared relative displacement

(MSRD), accounting for static σ_{st}^2 and thermal $\sigma^2(T)$ disorder effects (Sayers et al. (1971); Lee & Pendry (1975)). The sum in Eq. (5) is taken over groups of atoms located at different distances from the absorber.

For moderate disorder, when the distribution of interatomic distances becomes asymmetric, the EXAFS equation can be expressed using the cumulant decomposition (Bunker (1983); Dalba et al. (1993)). The cumulant model is often useful for the analysis of anharmonic and thermal expansion effects (Tranquada & Ingalls (1983); Fornasini et al. (2017)), nanoparticles (Clausen & Nørskov (2000); Sun et al. (2017)), and disordered materials (Dalba et al. (1995); Okamoto et al. (2002)).

Temperature-dependent MSRD $\sigma_{ij}^2(T)$ for the i-j pair of atoms with the mean-square displacement (MSD) amplitudes $\mathrm{MSD}_i(T)$ and $\mathrm{MSD}_j(T)$ are related as follows:

$$\sigma_{ij}^2(T) = \mathrm{MSD}_i(T) + \mathrm{MSD}_j(T) - 2\phi\sqrt{\mathrm{MSD}_i(T)}\sqrt{\mathrm{MSD}_j(T)}, \tag{7}$$

where ϕ is a dimensionless correlation parameter (Booth et al. (1995)). Note that for atoms located at large distances (in distant coordination shells), the correlation effects become negligible (Jeong et al. (2003); Sapelkin & Bayliss (2002)) so that the value of $\sigma_{ij}^2(T)$ can be used to estimate the sum of two mean-square displacement amplitudes. The MSD values are traditionally obtained from diffraction measurements or lattice dynamics calculations, but molecular dynamics (MD) simulations and reverse Monte Carlo analysis of EXAFS data can be also used for this purpose (Jonane et al. (2018)).

The analysis of the outer coordination shells using Eq. 6 is often inaccurate due to the presence of the MS contributions. In fact, when MS effects are taken into account, the number of scattering paths increases rapidly for distant shells resulting in a huge number of fitting parameters required. To illustrate this problem, three cases of the face-centered cubic (FCC) Fe, body-centered cubic (BCC) Ni, and hexagonal close-packed (HCP) Zn structures were consider (Fig. 5), and the numbers of unique (accounting for a structure symmetry) and total scattering paths were compared with those evaluated according to the Nyquist criterion [$N_{\mathrm{par}} = 2\Delta k \Delta R/\pi$ (Bordiga et al. (2013))] for a long EXAFS spectrum with $\Delta k = 20$ Å^{-1}, as a function of radial distance (cluster radius around the absorbing atom). Note that the Nyquist criterion estimates the maximum number of independent variables for EXAFS

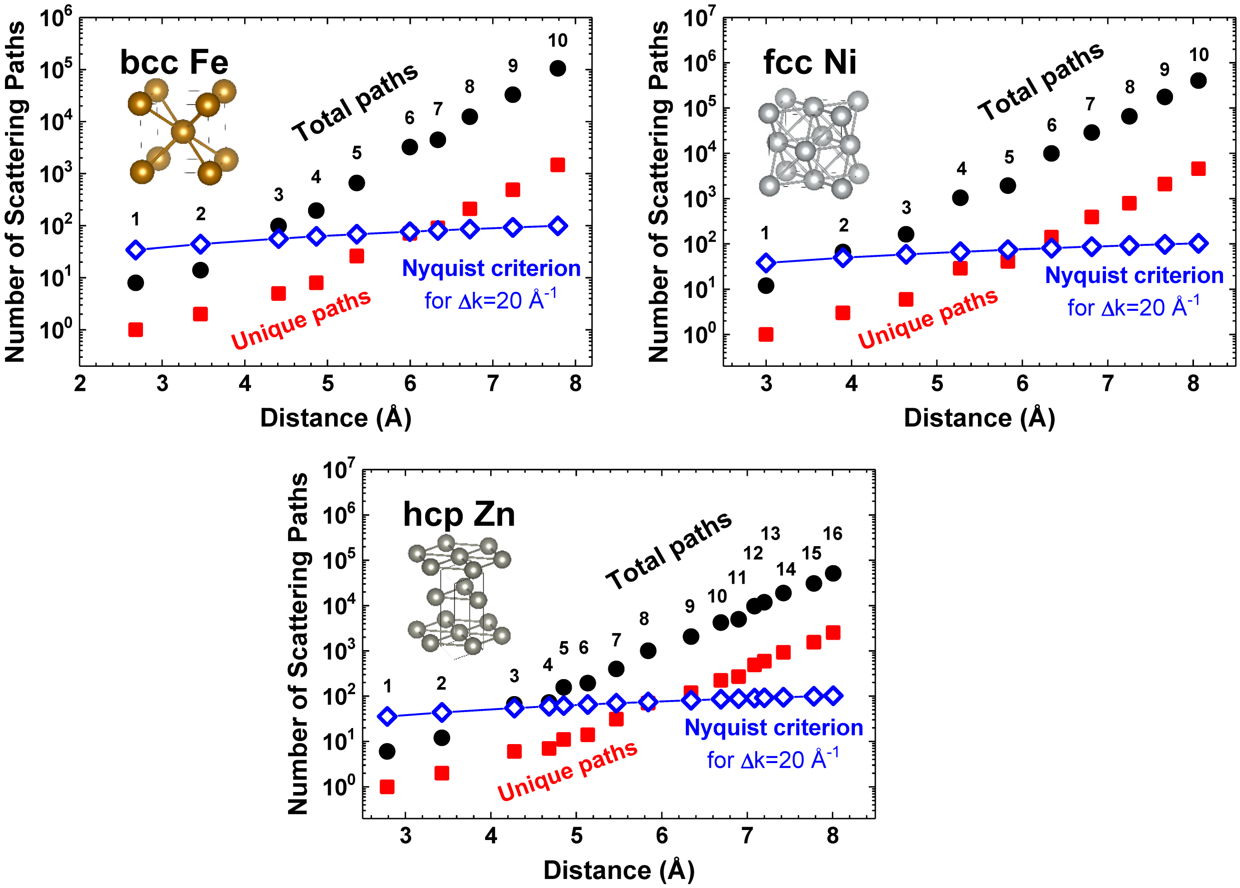

Figure 5: The dependence of the number of scattering paths on cluster size for the FCC Fe, BCC Ni, and HCP Zn structures. Solid circles – total number of paths, solid squares – unique number of paths, open diamonds – number of fitting parameters according to the Nyquist criterion. Note the logarithmic scale on the vertical axes. *BCC*, Body-centered cubic; *FCC*, face-centered cubic; *HCP*, hexagonal close-packed.

model. As one can see, the Nyquist criterion is not satisfied already at $R \sim 4$ Å when symmetry is broken as is in the case of HEAs due to the compositional disorder.

Note that only the effect of radial disorder is accounted in Eq. 6, while both scattering amplitude and phase shift functions of a photoelectron demonstrate non-linear angular dependence and are sensitive even to small variations of angles along the scattering path, especially in the case of linear atomic chains (Kuzmin & Purans (1993); Teo (1986)). This problem has been addressed in the past for small disorder using the low-order Taylor expansion for the amplitude and phase of the EXAFS signal (Filipponi et al. (1995); Filipponi & Di Cicco (1995)).

6.4. Advanced extended X-ray absorption fine structure analysis

To overcome the problems related to disorder effects and properly account for the MS contributions, the methods based on atomistic simulations (Fig. 6), such as MD (D'Angelo et al. (1994); Merkling et al. (2001); Cabaret et al. (2001); D'Angelo et al. (2002); Okamoto (2004); Farges et al. (2004); Ferlat et al. (2005); Kuzmin & Evarestov (2009); Price et al. (2012); Yancey et al. (2013)) and RMC (Winterer (2000); McGreevy (2001); Di Cicco & Trapananti (2005); Gereben et al. (2007); Krayzman et al. (2009); Krayzman & Levin (2010); Levin et al. (2014); Timoshenko et al. (2014c,b,a)), have been developed in the past. In both methods, the configuration-averaged (CA) EXAFS signal is calculated using coordinates of atoms obtained from one or more atomic configurations ("snapshots") during the simulation (Kuzmin et al. (2020)). It is important that these configurations naturally include both static and dynamic disorder. The CA-EXAFS spectra for different absorption edges can be calculated from the same set of atomic coordinates and used in the analysis. Note that in addition to atomic coordinates, two nonstructural parameters (ΔE_0 and S_0^2) should be also provided for comparison with experimental EXAFS spectra (Kuzmin & Chaboy (2014)). These parameters can be determined a priori by analyzing reference materials or by achieving the best match between experimental and calculated EXAFS spectra.

Apart from the similarities, there is also a principle difference between using MD and RMC methods to interpret EXAFS, which will be considered below.

6.4.1. Molecular Dynamics

In MD simulation, the 3D atomistic model of a material evolves for a fixed period of time following the trajectories which are determined by numerically solving classical Newton's equations of motion (Gale & Rohl (2003); Gowthaman (2023)). As a result, MD technique tends to be effective at high temperatures, enabling the modeling of the anharmonic motion of atoms. At the same time, the calculated amplitudes of thermal vibrations at low temperatures are underestimated due to a neglect of the zero-point (quantum) atomic motion (Markland & Ceriotti (2018); Yang & Kawazoe (2012)). To address this problem, alternative methods such as, for example, path integral MC or path integral MD, should be employed instead (Berne & Thirumalai (1986); Marx & Parrinello (1996); Tuckerman et al. (1996)).

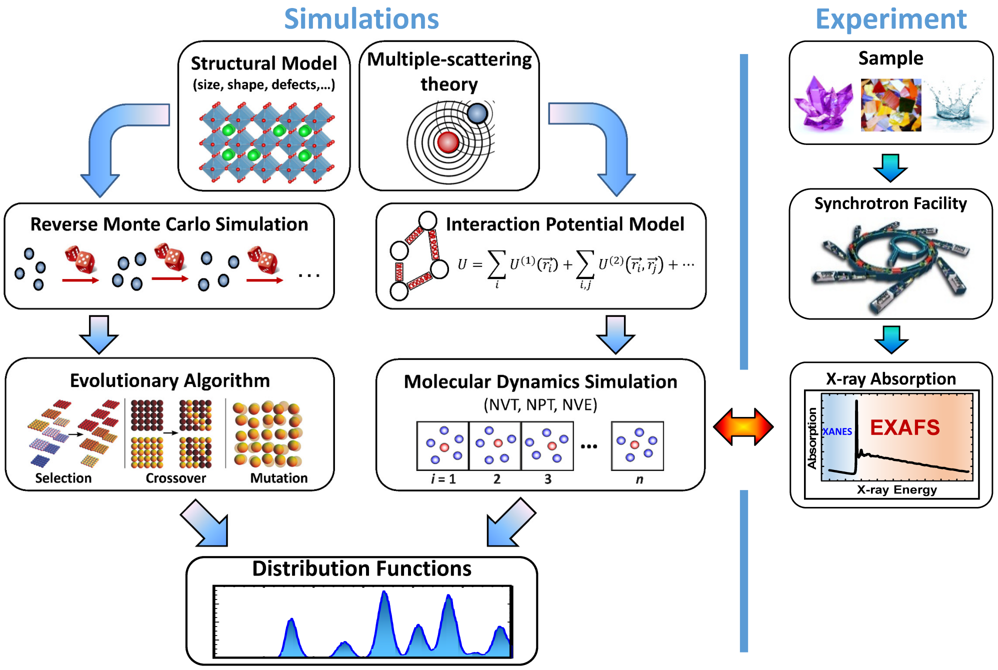

Figure 6: Scheme of EXAFS analysis using RMC and MD methods. The simulations are performed based on the initial structural model and the ab initio multiple-scattering formalism. In the case of the RMC approach, the agreement between the experimental and calculated data is used to optimize the structural model, while the configuration-averaged EXAFS spectrum obtained after MD simulation is employed to validate the interatomic potential model. In both cases, the atomic configurations are finally used to determine different distribution functions that describe the structure of a material, including disorder effects. *EXAFS*, Extended X-ray absorption fine structure; *MD*, molecular dynamics; *RMC*, reverse Monte Carlo.

MD simulations are performed using different ensembles (Abraham (1986)) such as the microcanonical ensemble (NVE), the canonical ensemble (NVT), or the isothermal-isobaric (NPT) ensemble, in which the number of atoms (N), the system's volume (V), the temperature (T), the pressure (P), or the energy (E) remain conserved during the simulation. The MD method provides a dynamic representation of the system's evolution, effectively simulating thermal disorder. Depending on the description of atomic interactions, the method can be classified as either classical or ab initio MD.

In classical MD, the forces between the atoms and their potential energies are calculated using empirically defined interatomic potentials (frequently called force fields). This significantly reduces the total computational time and required resources but allows one to model large systems, including millions of atoms on a long time-scale up to milliseconds

(Delaye (2001); Pierce et al. (2012)). At the same time, the reliability of such MD simulations depends directly on the accuracy of the empirical potential. Designing the interatomic potential is a complex task, involving choosing its functional form and obtaining a set of parameters on which it depends. Conventionally, two strategies are used to optimize the potential parameters: They are fitted to reproduce material properties such as structure, elastic constants, and phonon frequencies, or the potential-energy surface determined directly from ab initio density functional theory (DFT) simulations (Gale & Rohl (2003)).

The EXAFS spectrum, which includes information on both structural and dynamic disorder, represents an additional "property" that is well-suited for testing the quality of MD simulation or interatomic potentials. For this, a set of atomic configurations obtained during MD simulation is used to calculate the CA-EXAFS spectrum for an element of interest based on the ab initio multiple-scattering theory using, for example, FEFF (Ankudinov et al. (1998); Rehr et al. (2010)) or GNXAS (Filipponi & Di Cicco (2000)) code. It can then be compared with the experimental data, and the degree of agreement between the two EXAFS spectra can be used as a criterion to validate the interatomic potential model. Examples of such applications to $SrTiO_3$, ZnO, UO_2, BCC W, and ScF_3 can be found in (Bocharov et al. (2017, 2020); Jonane et al. (2018); Kuzmin & Evarestov (2009); Kuzmin et al. (2016)).

Machine learning (ML) (Behler (2016)) has recently emerged as an alternative method for representing potential-energy surfaces, wherein large datasets derived from electronic structure calculations are fitted. ML potentials combine the strengths of empirical potentials and first-principles models, making them a valuable tool for atomistic simulations. However, the need for verification of ML potentials remains. Recently, the accuracy of moment tensor potentials has been successfully validated by comparing the EXAFS spectra of four metals (BCC W and Mo, FCC Cu and Ni) obtained experimentally and computed from the results of MD simulations (Fig. 7) (Shapeev et al. (2022)). The method allows one to account for both SS and MS contributions to the total EXAFS spectrum while also considering disorder effects. This is important for achieving good agreement in the region of distant coordination shells (above 3.5–4 Å), especially in materials with many linear atomic chains in their structure, such as BCC and FCC metals. Note that the MS contributions extend over the entire k-range, whereas the MS peaks appear at long distances in the R-space due

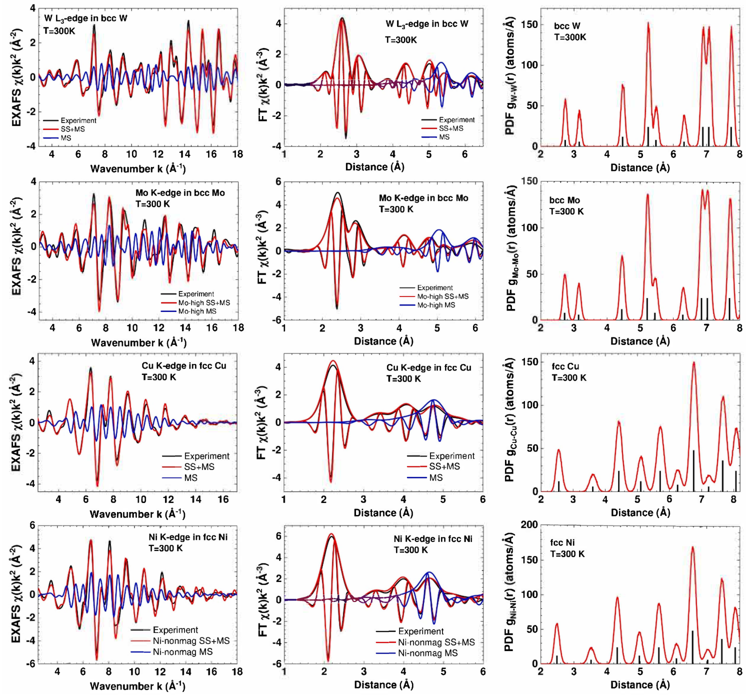

Figure 7: Comparison of the results of the MD–EXAFS simulations using the moment tensor potentials for BCC W and Mo and FCC Cu and Ni metals: the experimental and calculated EXAFS spectra (left panels) and their Fourier transforms (middle panels) at 300 K for BCC W and Mo and FCC Cu and Ni metals. The total calculated spectra, including SS and MS contributions, are shown by red lines, whereas the MS contributions are separately shown by blue lines. The PDFs $g(r)$ (*solid curves*) are given in the right panels together with the positions of crystallographic shells (*vertical bars*). *BCC*, Body-centered cubic; *EXAFS*, extended X-ray absorption fine structure; *FCC*, face-centered cubic; *MD*, molecular dynamics; *MS*, multiplescattering; *PDFs*, pair distribution functions; *SS*, single-scattering. From (Shapeev et al. (2022)). Copyright (2022), with permission from Elsevier.

to the large lengths of the MS paths.

6.4.2. Reverse Monte Carlo Simulations

The RMC simulation method employs a variation of the Metropolis algorithm (Metropolis et al. (1953)) and aims to identify an atomic configuration which is consistent with specific material properties, such as, for example, an EXAFS spectrum, neutron, or X-ray scattering data (Woicik et al. (2023)). It is important that the selected properties are directly connected to the material structure. In this scenario, the structural model is adjusted at each simulation step to match experimental data, and no information on interatomic potentials is required, which is an advantage over MD simulation.

The RMC method was originally proposed in the late 1980s as an approach to extract structural information such as atomic pair distribution functions from X-ray or neutron scattering data (Keen & McGreevy (1990); McGreevy & Pusztai (1988)). Shortly after, its application expanded to include the analysis of EXAFS spectra (Gurman & McGreevy (1990)). A recent review discussing the strengths and weaknesses of the method for the modeling of EXAFS data can be found in (Di Cicco & Iesari (2022)).

The use of the RMC method in EXAFS analysis additionally benefits from the sensitivity of EXAFS spectra to high-order atomic distribution functions, which contribute through MS effects (Rehr & Albers (2000)). This additional information, exclusively present in the EXAFS spectra, has a positive effect on the stability of the solution and, ultimately, on the reliability of the resulting structural model. Moreover, the element selectivity of XAS allows one to obtain experimental EXAFS spectra of different chemical elements present in a multicomponent compound independently. These spectra can be simultaneously employed in RMC simulation to determine a single structural model that is in agreement with all available experimental data.

In an RMC simulation, the model is represented by atoms placed according to the material density within a simulation box (often referred to as a cell or supercell) that matches the desired size and shape. Periodic boundary conditions (PBC) are commonly employed to mitigate surface-related effects. However, it is important to note that PBC imposes a limitation on the maximum cluster radius for EXAFS calculations, restricting it to half the minimum size of the box. This restriction helps to avoid the occurrence of artificial correlation effects.

During RMC simulation, the positions of all atoms in the box are typically randomly modified in each iteration (simulation step), and the CA–EXAFS signal is calculated. The decision to accept or reject the new atomic configuration is made based on the Metropolis algorithm, taking into account the difference (residual) between the experimental and simulated data in either k or R space, or both simultaneously through the wavelet transformation (Timoshenko & Kuzmin (2009)). Additionally, chemical or geometrical constraints can be incorporated into the residual value to prevent scenarios where atoms excessively approach or distance themselves from each other, certain bond angles acquire non-physical values, or unexpected deviations occur in the coordination number of specific atoms (Tucker et al. (2007)).

The efficiency of RMC simulation can be significantly improved using an evolutionary algorithm alongside a simulated annealing scheme (Timoshenko et al. (2014c, 2012)). The RMC technique is based on stochastic processes and typically converges towards the most disordered solution that aligns with the experimental data (Tucker et al. (2007)). Executing the simulation multiple times with various initial conditions yields distinct sets of final atomic coordinates, which are then used to obtain information about configuration-averaged atomic and bond-angle distribution functions.

To perform RMC analysis of EXAFS spectra, several software packages exist, including RMC-GNXAS (Di Cicco & Iesari (2022); Di Cicco & Trapananti (2005)), RMC++/RMC_POT (Gereben & Pusztai (2012); Gereben et al. (2007)), EvAX (Timoshenko et al. (2014c)), RMCProfile (Tucker et al. (2007); Zhang et al. (2020)), RMCXAS (Geiss et al. (2022); Winterer (2000)), m-RMC (Fujikawa et al. (2014)), EPSR-RMC (Bowron (2008)), and SpecSwap-RMC (Leetmaa et al. (2010)).

6.5. Applications to High-Entropy Materials

The use of XAS to investigate the local environment in HEMs dates back to 2009 (Chen et al. (2009)), but until recently it has been rather sporadic (Rost et al. (2015); Tamm et al. (2015); Maulik et al. (2017); Zhang et al. (2017, 2018); Braun et al. (2018); Harrington et al. (2019)). Most studies published in the past have been devoted to HEAs (Chen et al. (2009); Tamm et al. (2015); Maulik et al. (2017); Zhang et al. (2017, 2018); Fantin et al. (2020); Tan et al. (2021); He et al. (2021); Morris et al. (2021); Wu et al. (2021); Fantin et al. (2022); Smekhova et al. (2022a,b); Zhang & Song (2022); Pugliese et al. (2023); Tan et al. (2023); Smekhova et al. (2023); Gornakova et al. (2023)) and high entropy oxides (HEOs) (Rost et al. (2015); Braun et al. (2018); Ghigna et al. (2020); Tavani et al. (2020, 2021); Dupuy et al. (2021); Sushil et al. (2021); Han et al. (2022); Walczak et al. (2022); Luo et al. (2022); Wang et al. (2022); Molenda et al. (2023); Jacobson et al. (2023); Bakradze et al. (2023)), but a few works have been dedicated to high-entropy metal carbides (Harrington et al. (2019)), diborides (Gaboardi et al. (2022)), and metallic glasses (Zhang et al. (2022a)). Below several examples of XAS studies of HEA and HEO materials will be discussed.

It should be mentioned that the high concentration of principal elements in HEMs simplifies the measurement of their experimental X-ray absorption spectra. However, the compositional disorder and often proximity of the elements constituting HEM in the periodic table of elements make the analysis of these spectra challenging, requiring the use of simple structural models or specific constraints between model parameters. Therefore, existing and emerging advanced methods of data analysis will contribute greatly to the development of the field in the future.

6.5.1. High-Entropy Alloys

In the earlier study (Chen et al. (2009)), the authors successfully prepared a binary to octonary Cu-–Ni-–Al—Co-–Cr—Fe—Ti-–Mo alloy series using mechanical alloying (MA) and investigated their phase evolution and amorphisation behavior during milling. The formation of FCC and BCC structures was observed in the binary $\mathrm{Cu_{0.5}Ni}$ alloy and the ternary $\mathrm{Cu_{0.5}NiAl}$ alloy, respectively, both of which remained crystalline even after 60 h of milling. However, the FCC phase was first formed in the quaternary $\mathrm{Cu_{0.5}NiAlCo}$ alloy and alloys with more components, but it transformed into the amorphous phase after prolonged milling. Qualitative analysis of Fourier transformations of the Cu, Ni, Co, Cr, Fe, and Ti K-edge EXAFS spectra was employed to examine the local atomic configuration of each element in the alloys (Chen et al. (2009)). The presence or reduction of peaks in the FTs was used to confirm the formation of the FCC or amorphous phase (Chen et al. (2009)).

The SRO of equimolar ternary NiCrCo and quaternary NiCrCoFe alloys in the FCC phase was theoretically studied using a lattice MC method combined with DFT calculations by Tamm et al. (2015). The structural model consisted of a supercell with 108 atoms, and the MC simulation was followed by an MD run to allow for atomic relaxations. The MC simulations suggested a significant degree of SRO in both alloys compared to fully random distributions (Tamm et al. (2015)). Specifically, in the ternary NiCrCo alloy, a 40% decrease in the number of Cr–Cr pairs was observed, accompanied by an increase in the number of Ni–Cr and Cr–Co atom pairs (Tamm et al. (2015)). Similarly, the quaternary NiCrCoFe alloy exhibited a decrease in the number of Cr–Cr, Fe–Fe, Ni–Ni, and Co–Co pairs, along with an increase in Ni–Cr, Ni–Fe, Cr–Co, and Co–Fe atom pairs (Tamm et al. (2015)). An attempt was also made to validate the theoretical models using the experimental Fe K-edge EXAFS spectrum of the NiCrCoFe alloy. However, the difference between the calculated Fe K-edge EXAFS spectra for quasi-random and SRO structures was negligible, and both spectra aligned quite well with the experimental data (Tamm et al. (2015)).

The local atomic structure in a medium entropy alloy (MEA) NiCoCr was studied using three structural methods such as X-ray or neutron total scattering and XAS at the Cr, Co, and Ni K-edges in (Zhang et al. (2017)). Total scattering methods are complementary to XAS and provide the pair distribution functions (PDFs) extending up to 20–30 Å. However, the analysis of the total PDFs was not able to discriminate partials contributions and to evidence any detectable lattice distortion (Zhang et al. (2017)). At the same time, the SRO was revealed from the analysis of EXAFS spectra using the multicomponent analysis (Zhang et al. (2017)). It was found that the bond lengths and DW factors of Ni–Cr and Co–Cr pairs are different from those of Ni–Ni(Co) and Co–Co(Ni) pairs. Also, some evidence of the SRO enhancement by ion irradiation was proposed based on the EXAFS results (Zhang et al. (2017)). The local structure and lattice distortion in NiCoFeMnCr HEA were also studied by the same group (Zhang et al. (2018)). Independent analysis of the K-edge EXAFS spectra for five metallic elements indicates close (within the error reported) nearest interatomic distances of 2.53–2.54±0.01 Å and the DW factors of σ^2=0.007±0.001 Å^2 (Zhang et al. (2018)).

The local lattice distortions and their correlations with chemical compositions were investigated in CrCoNi MEA, CrFeCoNi and CrMnFeCoNi HEAs using synchrotron radiation based X-ray diffraction and EXAFS techniques by Tan et al. (2021). The distortion of the first coordination shell around each alloying element was estimated from the analysis of the EXAFS contribution from the first peak in the FTs (Tan et al. (2021)). The study revealed that the distortions are not severe and are highly element dependent, following the order of Ni $>$ Co $>$ Fe $>$ Cr $>$ Mn in all three alloys (Tan et al. (2021)). Additionally, the averaged strain around each alloying element was also calculated; it was positive around Ni, while, negative around Cr (Tan et al. (2021)). However, it is important to approach these findings with caution due to the simplicity of the model used.

To overcome the limitations of single-element catalysts, FeCoNiXRu (X = Cu, Cr, or Mn)

HEA nanoparticles with different active sites for water splitting in alkaline conditions were reported by Hao et al. (2022). The authors found that the Co and Ru sites in the HEA can simultaneously stabilize OH* and H* intermediates, thus enhancing the efficiency of water dissociation (Hao et al. (2022)). XAS was used to investigate the chemical states and bond structures of Co and Ru in the HEA before and after the stability test. The analysis of the Co and Ru K-edges XANES shows that Co and Ru are in metallic states and surrounded by different metallic species, suggesting the formation of a single-phase HEA (Hao et al. (2022)). The EXAFS results also confirm that Co and Ru keep their metallic states and bond lengths after the long-term stability test, demonstrating the excellent durability of the HEA catalyst (Hao et al. (2022)).

The local environment of six alloying elements in the $Al_8Cr_{17}Co_{17}Cu_8Fe_{17}Ni_{33}$ (at.%) compositionally complex alloy (CCA) with the FCC-type lattice was studied by Fantin et al. (2020). The analysis of the contribution of the first coordination shell to the metal K-edge EXAFS spectra, based on the multiparameter fit approach, allowed the determination of coordination numbers, interatomic distances, and DW factors. A higher affinity of Al for the heavier 3d metals, especially Cu, and the absence of Al-–Al pairs were discovered (Fantin et al. (2020)). Thus the EXAFS results indicated the presence of SRO in the alloy (Fantin et al. (2020)). A comparative analysis of the K-edge XANES in the alloy and pure metals suggested charge redistribution between Ni/Cu and Al due to orbital hybridization, which is responsible for the shrinkage of the Al metallic radius (Fantin et al. (2020)). In the subsequent study (Fantin et al. (2022)), the effect of heat treatment up to 1150°C on the $Al_8Cr_{17}Co_{17}Cu_8Fe_{17}Ni_{33}$ CCA was addressed, since the alloy exhibits a high temperature single-phase γ state above 900°C and a two-phase state with γ' precipitates below that temperature. A multi-edge analysis of the first coordination shell for each transition metal edge was performed, utilizing simultaneously two data sets for the transition metal and aluminium (Fantin et al. (2022)). Such an approach allows one to constrain the total coordination number to 12 nearest neighbours, as expected in the FCC lattice, and account for mixed coordination (Fantin et al. (2022)). The obtained results suggest that the heat treatment at 910°C, which is just above the γ' formation temperature, does not affect the microstructure, hardness, local atomic or electronic structure of the alloy (Fantin et al.

(2022)).

The combination of XAS with the RMC simulations was utilized to investigate the local crystallographic ordering and specific structural relaxations of each constituent in the equiatomic single-phase FCC CrMnFeCoNi (Cantor) HEA at room temperature (Fig. 8) by Smekhova et al. (2022a). The study demonstrated the reliability of the RMC method (Timoshenko et al. (2014c)) in analysing complex multicomponent systems like HEAs. This method enabled multi-edge analysis and simultaneous fitting of the same structural model to wavelet transforms (Timoshenko & Kuzmin (2009)) of all available experimental EXAFS spectra (Smekhova et al. (2022a)). Consequently, a set of partial and total distribution functions was generated for a detailed analysis from the final atomic configuration obtained in the RMC simulations. The findings revealed that all five elements of the alloy are distributed at the nodes of the FCC lattice with statistically similar averaged interatomic distances (2.54–2.55 Å), without exhibiting any signs of atomic-scale ordering (Smekhova et al. (2022a)). Notably, Cr atoms displayed larger structural displacements compared to the other elements, potentially influencing the magnetic properties of the alloy (Smekhova et al. (2022a)).

The same group (Smekhova et al. (2022b)) employed a similar approach to explore the Al-driven peculiarities of the local structure in single-phase FCC $Al_{0.3}$-CrFeCoNi and bcc Al_3-CrFeCoNi HEAs. The analysis of the Cr, Fe Co, and Ni K-edges EXAFS spectra by the RMC method revealed unimodal and bimodal distributions of all five elements, along with their correlation with the magnetic properties of the alloys (Smekhova et al. (2022b)). Furthermore, soft X-ray XANES at the $L_{2,3}$ -edges of the metals uncovered a degree of surface atoms oxidation, suggesting different kinetics of oxide formation for each type of constituents (Smekhova et al. (2022b)).

In a recent study (Smekhova et al. (2023)), element-specific XAS techniques were employed to probe the structural, electronic, and magnetic properties of individual constituents in a nanocrystalline $Cr_{20}Mn_{26}Fe_{18}Co_{19}Ni_{17}$ thin film with a single-phase FCC structure. The EXAFS analysis, using the RMC method, revealed a homogeneous short-range FCC atomic environment around each absorber with close interatomic distances (2.54-–2.55 Å) to their nearest-neighbors and enlarged structural relaxations of Cr atoms (Smekhova et al. (2023)).

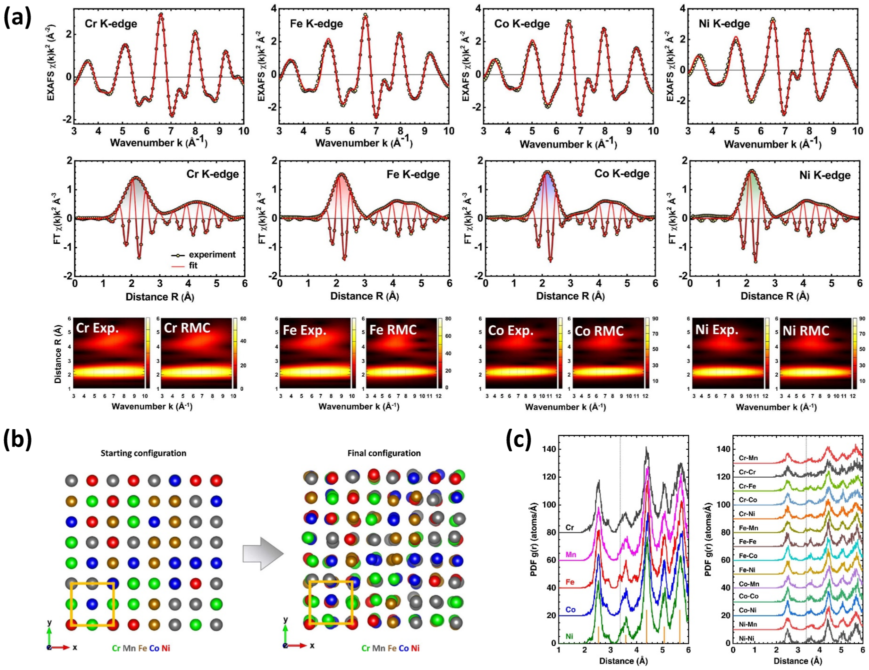

Figure 8: Analysis of the Cr, Fe, Co, and Ni K-edge EXAFS spectra of the FCC CrMnFeCoNi HEA at 300 K using the RMC method: (a) Comparison of the experimental and RMC-calculated Cr, Fe, Co, and Ni K-edge EXAFS spectra $\chi(k)k^2$ and their Fourier and Morlet wavelet transforms. (b) Starting and final atom configurations used in the RMC simulations for simultaneous fit to EXAFS spectra at four absorption edges. (c) Total and partial pair distribution functions (PDFs) $g(r)$ for the FCC CrMnFeCoNi HEA calculated from the final atom configuration. *EXAFS*, Extended X-ray absorption fine structure; *FCC*, face-centered cubic; *HEA*, high-entropy alloys; *PDFs*, pair distribution functions; *RMC*, reverseMonte Carlo. From (Smekhova et al. (2022a)). Copyright (2022), with permission from Elsevier.

The XANES analysis indicated that Cr and Mn atoms were oxidized at the surface, whereas Fe, Co, and Ni atoms remained predominantly metallic (Smekhova et al. (2023)). Furthermore, the analysis of X-ray magnetic circular dichroism spectra revealed that Fe, Co, and Ni atoms exhibit significant spin and orbital magnetic moments, whereas Cr and Mn atoms possess small magnetic signals with opposite signs (Smekhova et al. (2023)).

The element-specific local lattice distortions in the BCC TiZrHfNbTa refractory HEA were quantified before and after a tensile test using a combination of synchrotron radiation X-ray diffraction and EXAFS methods by Tan et al. (2023). The averaged atom pair distances obtained from diffraction patterns using Rietveld refinement and the distances for atom pairs determined from the Zr and Nb K-edge EXAFS spectra were used to estimate element specific local distortions (Tan et al. (2023)). It was found that the local environment around Zr experienced stronger distortion than that around Nb in the as-prepared HEA, and this distortion increases after the tensile test (Tan et al. (2023)).

A temperature-dependent Zr K-edge EXAFS study was conducted on polycrystalline superconductors by Pugliese et al. (2023), including $CoZr_2$ ($T_c = 6.2$ K), medium entropy $Co_{0.33}Rh_{0.34}Ir_{0.33}Zr_2$ ($T_c = 8.7$ K), and high entropy $Co_{0.2}Fe_{0.2}Ni_{0.2}Rh_{0.2}Ir_{0.2}Zr_2$ ($T_c = 5.3$ K). It was found that the temperature effect on the interatomic distances was marginal, however, an increase in static disorder around Zr was observed with increasing mixing entropy (Pugliese et al. (2023)). The temperature dependences of the EXAFS Debye-Waller factors for near neighbor distances, such as Zr–Co(Fe,Ni), Zr–Ir(Rh), Zr–Zr_1, Zr–Zr_2, Zr–Zr_3, were determined, demonstrating close behaviour except for the longest Zr–Zr_2 and Zr–Zr_3 bonds, which exhibited increased stiffness in the HEA (Pugliese et al. (2023)).

The influence of heat treatment and high-pressure torsion (HPT) on the structure of the TiZrHfMoCr high-entropy alloy was investigated by Gornakova et al. (2023). XAS was employed at the Ti, Cr, Zr, and Mo K-edges, as well as at the Hf L_3-edge, to probe the local atomic structure of two samples: one in the as-cast (AC) state and another after HPT treatment. The normalized XANES spectra of the HEAs (Fig. 9) indicate the similarity of the local environment around metal atoms before and after HPT treatment. A pre-edge peak (or shoulder) A arising from the $1s \rightarrow nd$ ($n = 3$ for Ti and Cr, n = 4 for Zr and Mo) transition (Muller et al. (1978); Müller et al. (1982)) is present in all K-edge XANES spectra. It becomes less prominent at higher excitation energies due to an increase in the natural line width of the 1s core level for heavier elements (Keski-Rahkonen & Krause (1974)). The strong resonance just above the Hf L_3-edge, known as the white line (WL), is produced by the dipole-allowed transition $2p_{3/2}$(Hf) $\rightarrow$5d (Qi et al. (1987)). The EXAFS results also indicated that the local environment around metal atoms was preserved after HPT, except for some increased static disorder, presumably in the grain boundary region (Gornakova et al. (2023)). Additionally, distinct local environments around Mo/Cr, Zr/Hf, and Ti atoms were revealed through the analysis of their EXAFS spectra, which were consistent with the crystallographic phases identified by XRD (Gornakova et al. (2023)).

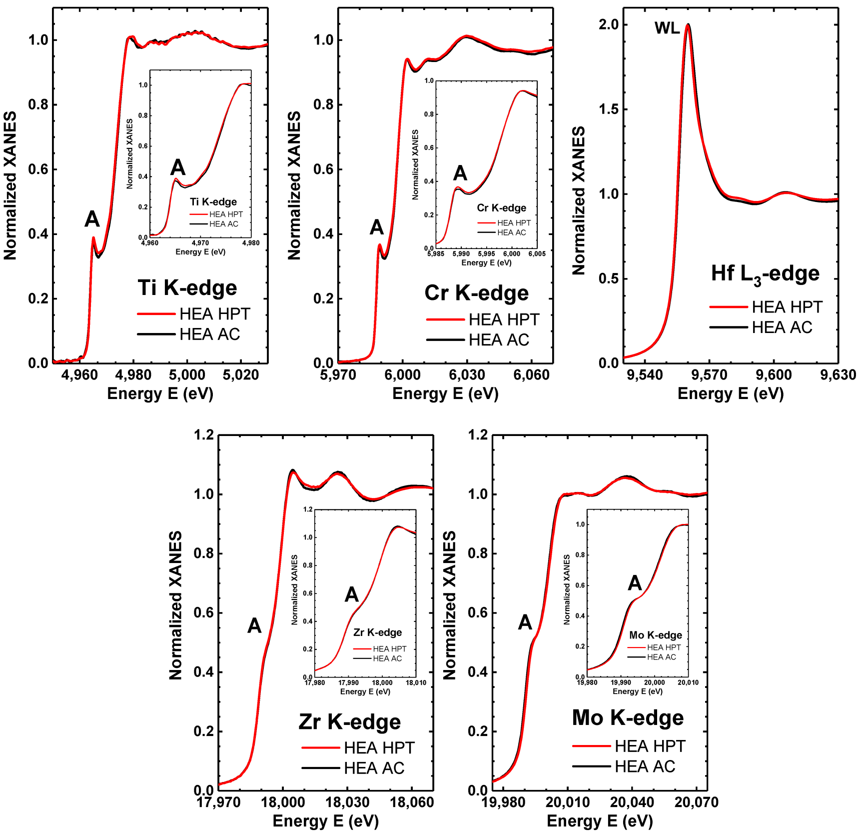

Figure 9: Normalized XANES spectra of TiZrHfMoCr HEA sample (as-cast (AC) and after high-pressure torsion (HPT) treatment) measured at the Ti, Cr, Zr, and Mo K-edges and Hf L_3-edge. The insets show an enlarged view around the absorption edge. The pre-edge peak A at K-edges and the white line (WL) at the L_3-edge are indicated. *AC*, As-cast; *HEA*, high-entropy alloys; *HPT*, high-pressure torsion; *WL*, white line; *XANES*, X-ray absorption near-edge structure. From (Gornakova et al. (2023)). Copyright (2023), with permission from MDPI.

6.5.2. High-Entropy Oxides

In a pioneering study of HEO (Rost et al. (2015)), five binary oxides were equimolarly mixed, forming an entropy-stabilized (Mg,Ni,Co,Cu,Zn)O system with the rock-salt structure, confirmed by diffraction. It is important to note that pure MgO, NiO, and CoO oxides have the crystal structures identical to HEO, but CuO and ZnO possess different tenorite and wurtzite structures, respectively. Therefore a structural transition takes place upon mixing (Rost et al. (2015)). EXAFS results obtained at the metal K-edges show that the local structures of each cation species in HEO are similar and consistent with a random cation distribution, supporting the entropy stabilization hypothesis (Rost et al. (2015)). The metal-to-oxygen nearest-neighbour distances for each metal species were found to be close within experimental error and comparable to the values reported for rocksalt structures (Rost et al. (2015)). The absence of SRO or clustering in HEO was demonstrated based on the shape of the EXAFS oscillations (Rost et al. (2015)).

In a subsequent study (Braun et al. (2018)), the effect of an additional sixth element (Sc, Sb, Sn, Cr, Ge) on the properties of the (Mg,Ni,Co,Cu,Zn)O system was investigated. It was observed that entropy-stabilized oxides have very low thermal conductivity and high elastic modulus attributed to a disorder in the interatomic forces caused by local ionic charge disorder (Braun et al. (2018)). The EXAFS results for the first and second coordination shells showed that the addition of a sixth cation to a five-cation HEO leads to a significant distortion of the oxygen sublattice and a change in the local coordination environment around the cobalt absorber (Braun et al. (2018)). These structural changes indicate that the ionic bonds in HEOs are highly disordered and affect the phonon scattering rate, which in turn determines the thermal conductivity (Braun et al. (2018)).

The lithiation/delithiation mechanism in the (Mg,Ni,Co,Cu,Zn)O HEO anode for application in Li-ion batteries was elaborated upon by Ghigna et al. (2020). It was shown that the insertion of lithium is a complex and irreversible process, resulting in the reduction of transition metals (Co, Ni, Cu, Zn) to their metallic state and the formation of an alloy with Li ions (Ghigna et al. (2020)). Operando XAS studies at the metal K-edges supported this finding by demonstrating the changes in the local structure and oxidation state of the metal cations during the lithiation/delithiation process (Ghigna et al. (2020)). The multivariate curve resolution (MCR) and principal component analysis (PCA) methods were employed to quantitatively determine the number and identity of key metal-related species that appear during the HEO anode evolution and to monitor their concentration changes throughout the reaction (Tavani et al. (2020)). XANES and EXAFS results also revealed that the HEO rock-salt structure collapses after a certain degree of lithiation, leading to the segregation of metals and oxides (Ghigna et al. (2020)).

In the recent paper, the XAS method was employed to further advance our understanding of the behaviour of the (Mg,Ni,Co,Cu,Zn)O HEO during electrochemical cycling with lithium (Wang et al. (2023)). The remarkable electrochemical performance was demonstrated to result from the synergetic effect of the cations in the HEO during the conversion reaction with lithium. The analysis of the Co, Ni, Cu, and Zn K-edge XANES and EXAFS spectra revealed that the metal ions in the HEO are reduced to metallic state during the initial discharge, forming FCC Co, Ni, and Cu phases, as well as an FCC LiZn alloy (Wang et al. (2023)). After recharging to 3.0 V, the metal ions exhibit different behaviors: Ni and Cu remain in the metallic state, whereas a significant fraction of Co participates in the redox reaction, with some Co remaining in a metallic state. Zn is almost fully deoxidized to the 2+ state (Wang et al. (2023)). Thus, the elements with higher electronegativity (Cu and Ni) are responsible for creating an electrochemically inert conductive network, whereas the Zn cations stabilize an oxide nanophase, allowing for the accommodation of lithium ions (Wang et al. (2023)).

A novel catalyst (Pd_1@HEFO), combining Pd single-atom with a high-entropy fluorite oxide $(CeZrHfTiLa)O_x$ (HEFO) used as a support, was synthesized using a mechanochemical-assisted method by Xu et al. (2020). It demonstrated superior CO oxidation activity as well as thermal and hydrothermal stability compared to a conventional Pd@CeO_2 catalyst. The formation of single Pd atoms was confirmed by an atomic-resolution transmission electron microscopy image and the energy-dispersive X-ray spectroscopy mapping image of Pd (Xu et al. (2020)). XANES and EXAFS measurements performed at the Pd K-edge were used to confirm the formation of single Pd atoms in Pd_1@HEFO and to investigate their electronic structure and coordination environment (Xu et al. (2020)). The EXAFS spectra showed that the Pd atoms are incorporated into the HEFO sublattice by forming stable Pd–O–M bonds (M = Ce, Zr, La), with no Pd–Pd or Pd–O–Pd bonding (Xu et al. (2020)). The XANES results revealed that the valence state of Pd ranges between 0 and +2. These features contribute to the enhanced catalytic performance of Pd_1@HEFO (Xu et al. (2020)).

A cobalt-free spinel $(CrMnFeNiCu)_3O_4$ HEO is a candidate for the use as an anode material in lithium-ion batteries. Its charge–discharge mechanism was studied using operando quick-scanning XAS by Luo et al. (2022). Valence and coordination states of transition metal elements were determined from the edge positions and shapes of their K-edge XANES spectra. The results reveal that all the constituent elements (Cr, Mn, Fe, Ni, and Cu) in the HEO participate in the redox reactions during Li^+ uptake/release, but with different transition steps, redox sequence, reversibility, and overpotential (Luo et al. (2022)).

The concept of high entropy was employed by Han et al. (2022) to synthesize nanoporous NiFeCoMnAl oxide with an amorphous structure on carbon paper through electrochemical deposition followed by the dealloying technique aimed at reducing the amount of aluminium and creating a nanoporous structure. This HEO was proposed as an efficient electrocatalyst for the oxygen evolution reaction (OER) (Han et al. (2022)). The authors attributed the high OER activity to the synergistic effect of multiple elements, especially Mn doping, which promoted the formation of β-NiOOH intermediates with higher intrinsic activity compared to γ-NiOOH intermediates. The Ni K-edge XANES and EXAFS were employed to understand the influence of Mn doping on the valence state of nickel ions in NiFeCoMnAl before and after OER (Han et al. (2022)). The emergence of a higher oxidation state of Ni and shorter Ni–O distances after the OER were observed (Han et al. (2022)).

A medium-entropy (MnNiCuZn)WO_4 and high-entropy (MnCoNiCuZn)WO_4 tungstates with monoclinic crystal structure and a random distribution of 3d metal cations were recently synthesized (Bakradze et al. (2023)) and demonstrated different degree of local structure distortions. The XANES spectra at the Mn, Co, Ni, and Zn K-edges of both the medium-entropy tungstate (MET) and the high-entropy tungstate (HET) exhibit shapes similar to those found in pure tungstates, indicating a resemblance in the local atomic environment around each of these metal ions and the proximity of their oxidation states (Bakradze et al. (2023)). However, the Cu K-edge XANES spectra of the MET and the HET differ from that of $CuWO_4$, suggesting differences in the distortion of the copper environment (Bakradze et al. (2023)). EXAFS spectroscopy, combined with RMC simulations, allowed for a detailed examination of the atomic environments around metal cations in these compounds by determining the partial RDFs for metal-oxygen distances (Fig. 10) (Bakradze et al. (2023)). The EXAFS analysis revealed that Ni^{2+} ions have the strongest tendency to organize their local environment and form regular [NiO_6] octahedra, whereas Mn^{2+}, Co^{2+}, Zn^{2+}, and W^{6+} ions exhibit distorted octahedral coordination (Bakradze et al. (2023)). Perhaps the most intriguing result is that the shape of [CuO_6] octahedra in both tungstates differs from that in pure $CuWO_4$, where a strong Jahn–Teller distortion is present (Bakradze et al. (2023)). The authors proposed that the increase in configurational entropy indirectly affects the longest

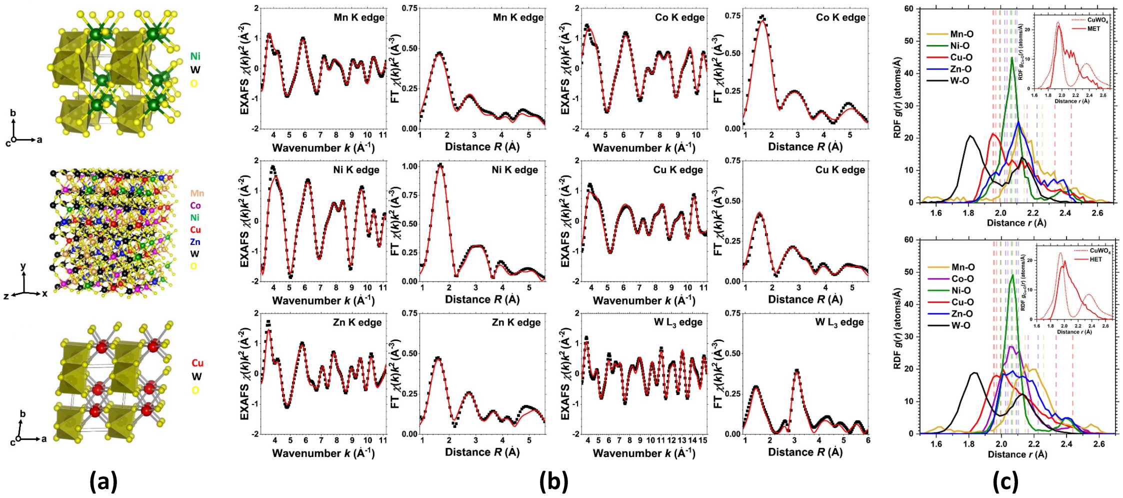

Figure 10: Results of the EXAFS study of MET (MnNiCuZn)WO$_4$ and HET (MnCoNiCuZn)WO$_4$ at 10 K using the RMC method: (a) Crystallographic structures of monoclinic NiWO$_4$, monoclinic (MnCoNiCuZn)WO$_4$, and triclinic CuWO$_4$. (b) Experimental (*black dots*) and calculated (*red lines*) EXAFS spectra $\chi(k)k^2$ and their Fourier transforms (FTs) for HET (MnCoNiCuZn)WO$_4$ at K-edges of Mn, Co, Ni, Cu, and Zn, and at the L$_3$-edge of W at 10 K. (c) Radial distribution functions (RDFs) $g(r)$ in (MnNiCuZn)WO$_4$ MET and (MnCoNiCuZn)WO$_4$ HET at 10 K. Vertical dashed lines indicate the respective bond lengths in pure MnWO$_4$, CoWO$_4$, NiWO$_4$, CuWO$_4$, and ZnWO$_4$ as determined by X-ray diffraction at 300 K. The inset shows partial RDFs for Cu–O atomic pairs in CuWO$_4$ and (MnNiCuZn)WO$_4$ or (MnCoNiCuZn)WO$_4$. *EXAFS*, Extended X-ray absorption fine structure; *FTs*, Fourier transforms; *HET*, high-entropy tungstate; *MET*, medium-entropy tungstate; *RDFs*, radial distribution functions; *RMC*, reverse Monte Carlo. From (Bakradze et al. (2023)). Copyright (2023), with permission from Elsevier.

Cu–O bonds in [CuO$_6$] octahedra (Bakradze et al. (2023)).

6.6. Conclusions

XAS provides a great opportunity to study the local environment in multicomponent compounds such as HEMs. By tuning the X-ray energy across the absorption edge of each element in HEM, information on their oxidation state, chemical bonding, and local structural distortions can be obtained. However, care should be taken when analysis is extended beyond the nearest coordination shell(s), since MS contributions originating from many-atom distributions may become important and, thus, should be taken into account in the analysis. The similarity of atomic scattering amplitudes can also be a limiting factor when HEM include elements neighboring in the periodic table, such as in Cantor alloys.

The use of advanced methods of EXAFS analysis based on atomistic simulations (Ferrari et al. (2020)) opens up many additional opportunities. The EXAFS spectra can be used to validate MD simulations, allowing the selection and optimization of potential models. The RMC method allows one to perform multi-edge EXAFS analysis and to determine a structural model of HEM being in agreement with all available experimental EXAFS spectra. This provides the possibility of obtaining a set of partial distribution functions that can be used further to determine such structural parameters as average interatomic distances, MSRDs for pairs of atoms, and mean-squared displacements for atoms of each type.

Further development of methods for analyzing XANES/EXAFS spectra, such as ML techniques (Timoshenko et al. (2017); Liu et al. (2023)), is expected to offer new opportunities for obtaining information on the local structure and its distortion in HEMs.

Acknowledgment

This work was supported by the Latvian Council of Science project No. lzp-2023/1-0476.

References

Abraham, F. F. (1986). Computational statistical mechanics methodology, applications and supercomputing. *Adv. Phys.*, *35*, 1–111. doi:`10.1080/00018738600101851`.

Albedwawi, S. H., AlJaberi, A., Haidemenopoulos, G. N., & Polychronopoulou, K. (2021). High entropy oxides-exploring a paradigm of promising catalysts: A review. *Mater. Des.*, *202*, 109534. doi:`10.1016/j.matdes.2021.109534`.

Ankudinov, A. L., Ravel, B., Rehr, J. J., & Conradson, S. D. (1998). Real-space multiple-scattering calculation and interpretation of X-ray-absorption near-edge structure. *Phys. Rev. B*, *58*, 7565–7576. doi:`10.1103/PhysRevB.58.7565`.

Bakradze, G., Welter, E., & Kuzmin, A. (2023). Peculiarities of the local structure in new medium- and high-entropy, low-symmetry tungstates. *J. Phys. Chem. Solids*, *172*, 111052. doi:`10.1016/j.jpcs.2022.111052`.

Behler, J. (2016). Perspective: Machine learning potentials for atomistic simulations. *J. Chem. Phys.*, *145*. doi:`10.1063/1.4966192`.

Berne, B. J., & Thirumalai, D. (1986). On the simulation of quantum systems: path integral methods. *Ann. Rev. Phys. Chem.*, *37*, 401–424. doi:`10.1146/annurev.pc.37.100186.002153`.

Bocharov, D., Chollet, M., Krack, M., Bertsch, J., Grolimund, D., Martin, M., Kuzmin, A., Purans, J., & Kotomin, E. (2017). Analysis of the U L_3-edge X-ray absorption spectra in UO_2 using molecular dynamics simulations. *Prog. Nucl. Energy*, *94*, 187–193. doi:`10.1016/j.pnucene.2016.07.017`.

Bocharov, D., Krack, M., Rafalskij, Y., Kuzmin, A., & Purans, J. (2020). Ab initio molecular dynamics simulations of negative thermal expansion in ScF_3: The effect of the supercell size. *Comput. Mater. Sci.*, *171*, 109198. doi:`10.1016/j.commatsci.2019.109198`.

Booth, C. H., Bridges, F., Bauer, E. D., Li, G. G., Boyce, J. B., Claeson, T., Chu, C. W., & Xiong, Q. (1995). XAFS measurements of negatively correlated atomic displacements in $HgBa_2CuO_4 + \delta$. *Phys. Rev. B*, *52*, R15745–R15748. doi:`10.1103/PhysRevB.52.R15745`.

Bordiga, S., Groppo, E., Agostini, G., van Bokhoven, J. A., & Lamberti, C. (2013). Reactivity of surface species in heterogeneous catalysts probed by in situ X-ray absorption techniques. *Chem. Rev.*, *113*, 1736–1850. doi:`10.1021/cr2000898`.

Bowron, D. T. (2008). Experimentally consistent atomistic modeling of bulk and local structure in liquids and disordered materials by empirical potential structure refinement. *Pure Appl. Chem.*, *80*, 1211–1227. doi:`10.1351/pac200880061211`.

Braun, J. L., Rost, C. M., Lim, M., Giri, A., Olson, D. H., Kotsonis, G. N., Stan, G., Brenner, D. W., Maria, J.-P., & Hopkins, P. E. (2018). Charge-induced disorder controls the thermal conductivity of entropy-stabilized oxides. *Adv. Mater.*, *30*, 1805004. doi:`10.1002/adma.201805004`.

Brechtl, J., & Liaw, P. K. (Eds.) (2021). *High-Entropy Materials: Theory, Experiments, and Applications*. Springer Cham. doi:`10.1007/978-3-030-77641-1`.

Buckingham, M. A., Ward-O'Brien, B., Xiao, W., Li, Y., Qu, J., & Lewis, D. J. (2022). High entropy metal chalcogenides: synthesis, properties, applications and future directions. *Chem. Commun.*, *58*, 8025–8037. doi:`10.1039/D2CC01796B`.

Bunker, G. (1983). Application of the ratio method of EXAFS analysis to disordered systems. *Nucl. Instrum. Methods*, *207*, 437–444. doi:`10.1016/0167-5087(83)90655-5`.

Cabaret, D., Grand, M. L., Ramos, A., Flank, A.-M., Rossano, S., Galoisy, L., Calas, G., & Ghaleb, D. (2001). Medium range structure of borosilicate glasses from Si K-edge XANES: a combined approach based on multiple scattering and molecular dynamics calculations. *J. Non-Cryst. Solids*, *289*, 1–8. doi:`10.1016/S0022-3093(01)00733-5`.

Cantor, B., Chang, I., Knight, P., & Vincent, A. (2004). Microstructural development in equiatomic multicomponent alloys. *Mater. Sci. Eng. A*, *375-377*, 213–218. doi:`10.1016/j.msea.2003.10.257`.

Cavin, J., Ahmadiparidari, A., Majidi, L., Thind, A. S., Misal, S. N., Prajapati, A., Hemmat, Z., Rastegar, S., Beukelman, A., Singh, M. R., Unocic, K. A., Salehi-Khojin, A., &

Mishra, R. (2021). 2D high-entropy transition metal dichalcogenides for carbon dioxide electrocatalysis. *Adv. Mater.*, *33*, 2100347. doi:`10.1002/adma.202100347`.

Chen, H., Li, S., Huang, S., Ma, L., Liu, S., Tang, F., Fang, Y., & Dai, P. (2022). High-entropy structure design in layered transition metal dichalcogenides. *Acta Mater.*, *222*, 117438. doi:`10.1016/j.actamat.2021.117438`.

Chen, Y.-L., Hu, Y.-H., Tsai, C.-W., Hsieh, C.-A., Kao, S.-W., Yeh, J.-W., Chin, T.-S., & Chen, S.-K. (2009). Alloying behavior of binary to octonary alloys based on Cu–Ni–Al–Co–Cr–Fe–Ti–Mo during mechanical alloying. *J. Alloys Compd.*, *477*, 696–705. doi:`10.1016/j.jallcom.2008.10.111`.

Clausen, B. S., & Nørskov, J. K. (2000). Asymmetric pair distribution functions in catalysts. *Top. Catal.*, *10*, 221–230. doi:`10.1023/A:1019196908404`.

Dalba, G., Fornasini, P., Grazioli, M., & Rocca, F. (1995). Local disorder in crystalline and amorphous germanium. *Phys. Rev. B*, *52*, 11034–11043. doi:`10.1103/PhysRevB.52.11034`.

Dalba, G., Fornasini, P., & Rocca, F. (1993). Cumulant analysis of the extended X-ray-absorption fine structure of β-AgI. *Phys. Rev. B*, *47*, 8502–8514. doi:`10.1103/PhysRevB.47.8502`.

D'Angelo, P., Barone, V., Chillemi, G., Sanna, N., Meyer-Klaucke, W., & Pavel, N. V. (2002). Hydrogen and higher shell contributions in Zn^{2+}, Ni^{2+}, and Co^{2+} aqueous solutions: an X-ray absorption fine structure and molecular dynamics study. *J. Am. Chem. Soc.*, *124*, 1958–1967. doi:`10.1021/ja015685x`.

D'Angelo, P., Di Nola, A., Filipponi, A., Pavel, N. V., & Roccatano, D. (1994). An extended x-ray absorption fine structure study of aqueous solutions by employing molecular dynamics simulations. *J. Chem. Phys.*, *100*, 985–994. doi:`10.1063/1.466581`.

Delaye, J.-M. (2001). Modeling of multicomponent glasses: a review. *Curr. Opin. Solid State Mater. Sci.*, *5*, 451–454. doi:`10.1016/S1359-0286(01)00028-6`.

Di Cicco, A. (1995). EXAFS multiple-scattering data-analysis: GNXAS methodology and applications. *Physica B*, *208-209*, 125–128. doi:`10.1016/0921-4526(94)00647-E`.

Di Cicco, A., & Iesari, F. (2022). Advances in modelling X-ray absorption spectroscopy data using reverse Monte Carlo. *Phys. Chem. Chem. Phys.*, *24*, 6988–7000. doi:`10.1039/D1CP05525A`.

Di Cicco, A., & Trapananti, A. (2005). Reverse Monte Carlo refinement of molecular and condensed systems by X-ray absorption spectroscopy. *J. Phys.: Condens. Matter*, *17*, S135–S144. doi:`10.1088/0953-8984/17/5/014`.

Dupuy, A. D., Chiu, I.-T., Shafer, P., Arenholz, E., Takamura, Y., & Schoenung, J. M. (2021). Hidden transformations in entropy-stabilized oxides. *J. Eur. Ceram. Soc.*, *41*, 6660–6669. doi:`10.1016/j.jeurceramsoc.2021.06.014`.

Fan, Z., Wang, H., Wu, Y., Liu, X. J., & Lu, Z. P. (2016). Thermoelectric high-entropy alloys with low lattice thermal conductivity. *RSC Adv.*, *6*, 52164–52170. doi:`10.1039/C5RA28088E`.

Fantin, A., Cakir, C., Kasatikov, S., Schumacher, G., & Manzoni, A. (2022). Effects of heat treatment on microstructure, hardness and local structure in a compositionally complex alloy. *Mater. Chem. Phys.*, *276*, 125432. doi:`10.1016/j.matchemphys.2021.125432`.

Fantin, A., Lepore, G. O., Manzoni, A. M., Kasatikov, S., Scherb, T., Huthwelker, T., d'Acapito, F., & Schumacher, G. (2020). Short-range chemical order and local lattice distortion in a compositionally complex alloy. *Acta Mater.*, *193*, 329–337. doi:`10.1016/j.actamat.2020.04.034`.

Farges, F., Lefrere, Y., Rossano, S., Berthereau, A., Calas, G., & Jr., G. E. B. (2004). The effect of redox state on the local structural environment of iron in silicate glasses: a combined XAFS spectroscopy, molecular dynamics, and bond valence study. *J. Non-Cryst. Solids*, *344*, 176–188. doi:`10.1016/j.jnoncrysol.2004.07.050`.

Ferlat, G., Soetens, J.-C., Miguel, A. S., & Bopp, P. A. (2005). Combining extended X-ray absorption fine structure with numerical simulations for disordered systems. *J. Phys.: Condens. Matter*, *17*, S145. doi:`10.1088/0953-8984/17/5/015`.

Ferrari, A., Dutta, B., Gubaev, K., Ikeda, Y., Srinivasan, P., Grabowski, B., & Körmann, F. (2020). Frontiers in atomistic simulations of high entropy alloys. *J. Appl. Phys.*, *128*, 150901. doi:`10.1063/5.0025310`.

Filipponi, A., & Di Cicco, A. (1995). X-ray-absorption spectroscopy and n-body distribution functions in condensed matter. II. Data analysis and applications. *Phys. Rev. B*, *52*, 15135–15149. doi:`10.1103/PhysRevB.52.15135`.

Filipponi, A., & Di Cicco, A. (2000). GNXAS: a software package for advanced EXAFS multiple-scattering calculations and data-analysis. *TASK Q.*, *4*, 575–669.

Filipponi, A., Di Cicco, A., & Natoli, C. R. (1995). X-ray-absorption spectroscopy and n-body distribution functions in condensed matter. I. Theory. *Phys. Rev. B*, *52*, 15122–15134. doi:`10.1103/PhysRevB.52.15122`.

Fornasini, P., Grisenti, R., Dapiaggi, M., Agostini, G., & Miyanaga, T. (2017). Nearest-neighbour distribution of distances in crystals from extended X-ray absorption fine structure. *J. Chem. Phys.*, *147*, 044503. doi:`10.1063/1.4995435`.

Fujikawa, K., Ariga, H., Takakusagi, S., Uehara, H., Ohba, T., & Asakura, K. (2014). Micro Reverse Monte Carlo approach to EXAFS analysis. *e-J. Surf. Sci. Nanotechnol.*, *12*, 322–329. doi:`10.1380/ejssnt.2014.322`.

Gaboardi, M., Monteverde, F., Saraga, F., Aquilanti, G., Feng, L., Fahrenholtz, W., & Hilmas, G. (2022). Local structure in high-entropy transition metal diborides. *Acta Mater.*, *239*, 118294. doi:`10.1016/j.actamat.2022.118294`.

Gale, J. D., & Rohl, A. L. (2003). The General Utility Lattice Program (GULP). *Mol. Simul.*, *29*, 291–341. doi:`10.1080/0892702031000104887`.

Geiss, J., Schulte, J., & Winterer, M. (2022). Flash evaporation of low volatility solid precursors by a scanning infrared laser. *J. Nanopart. Res.*, *24*, 248. doi:`10.1007/s11051-022-05611-3`.

George, E., Raabe, D., & Ritchie, R. (2019). High-entropy alloys. *Nat. Rev. Mater.*, *4*, 515–534. doi:`10.1038/s41578-019-0121-4`.

Gereben, O., Jovari, P., Temleitner, L., & Pusztai, L. (2007). A new version of the RMC++ Reverse Monte Carlo programme, aimed at investigating the structure of covalent glasses. *J. Optoelectron. Adv. M.*, *9*, 3021–3027.

Gereben, O., & Pusztai, L. (2012). RMC_POT: a computer code for reverse Monte Carlo modeling the structure of disordered systems containing molecules of arbitrary complexity. *J. Comput. Chem.*, *33*, 2285–2291. doi:`10.1002/jcc.23058`.

Ghigna, P., Airoldi, L., Fracchia, M., Callegari, D., Anselmi-Tamburini, U., D'Angelo, P., Pianta, N., Ruffo, R., Cibin, G., de Souza, D. O., & Quartarone, E. (2020). Lithiation mechanism in high-entropy oxides as anode materials for Li-ion batteries: An operando XAS study. *ACS Appl. Mater. Interfaces*, *12*, 50344–50354. doi:`10.1021/acsami.0c13161`.

Gornakova, A., Straumal, B., Kuzmin, A., Tyurin, A., Chernyaeva, E., Druzhinin, A., Afonikova, N., & Davdian, G. (2023). Influence of heat treatment and high-pressure torsion on phase transformations in TiZrHfMoCr high-entropy alloy. *Metals*, *13*, 1030. doi:`10.3390/met13061030`.

Gowthaman, S. (2023). A review on mechanical and material characterisation through molecular dynamics using large-scale atomic/molecular massively parallel simulator (LAMMPS). *Funct. Compos. Struct.*, *5*, 012005. doi:`10.1088/2631-6331/acc3d5`.

Gurman, S. J., & McGreevy, R. L. (1990). Reverse Monte Carlo simulation for the analysis of EXAFS data. *J. Phys.: Condens. Matter*, *2*, 9463–9473. doi:`10.1088/0953-8984/2/48/001`.

Han, M., Wang, C., Zhong, J., Han, J., Wang, N., Seifitokaldani, A., Yu, Y., Liu, Y., Sun, X., Vomiero, A., & Liang, H. (2022). Promoted self-construction of β-NiOOH in amorphous high entropy electrocatalysts for the oxygen evolution reaction. *Appl. Catal. B*, *301*, 120764. doi:`10.1016/j.apcatb.2021.120764`.

Hao, J., Zhuang, Z., Cao, K., Gao, G., Wang, C., Lai, F., Lu, S., Ma, P., Dong, W., Liu, T., Du, M., & Zhu, H. (2022). Unraveling the electronegativity-dominated intermediate adsorption on high-entropy alloy electrocatalysts. *Nat. Commun.*, *13*, 2662. doi:`10.1038/s41467-022-30379-4`.

Harrington, T. J., Gild, J., Sarker, P., Toher, C., Rost, C. M., Dippo, O. F., McElfresh, C., Kaufmann, K., Marin, E., Borowski, L., Hopkins, P. E., Luo, J., Curtarolo, S., Brenner, D. W., & Vecchio, K. S. (2019). Phase stability and mechanical properties of novel high entropy transition metal carbides. *Acta Mater.*, *166*, 271–280. doi:`10.1016/j.actamat.2018.12.054`.

He, H., Wang, B., Lan, S., Ruff, J. P. C., Sun, C., Naeem, M., Liu, C.-T., & Wang, X.-L. (2021). Anomalous X-ray scattering and extended X-ray absorption fine structure study of the local structure of CrFeCoNiMo$_x$ (x = 0.11, 0.18, and 0.23) high-entropy alloys. *JOM*, *73*, 3285–3290. doi:`10.1007/s11837-021-04871-z`.

Hu, J., Cao, L., Wang, Z., Liu, J., Zhang, J., Cao, Y., Lu, Z., & Cheng, H. (2021). Hollow high-entropy metal organic framework derived nanocomposite as efficient electrocatalyst for oxygen reduction reaction. *Compos. Commun.*, *27*, 100866. doi:`10.1016/j.coco.2021.100866`.

Huang, Y., Yeh, J.-W., & Yang, A. C.-M. (2021). "High-entropy polymers": A new route of polymer mixing with suppressed phase separation. *Materialia*, *15*, 100978. doi:`10.1016/j.mtla.2020.100978`.

Jacobson, V., Huang, J., Titus, C., Smaha, R., Papac, M., Lee, S., Zakutayev, A., & Brennecka, G. (2023). The role of Co valence in charge transport in the entropy-stabilized oxide ($Mg_{0.2}Co_{0.2}Ni_{0.2}Cu_{0.2}Zn_{0.2}$)O. *J. Am. Ceram. Soc.*, *106*, 1531–1539. doi:`10.1111/jace.18820`.

Jeong, I.-K., Heffner, R. H., Graf, M. J., & Billinge, S. J. L. (2003). Lattice dynamics and correlated atomic motion from the atomic pair distribution function. *Phys. Rev. B*, *67*, 104301. doi:`10.1103/PhysRevB.67.104301`.

Jonane, I., Anspoks, A., & Kuzmin, A. (2018). Advanced approach to the local structure reconstruction and theory validation on the example of the W L_3-edge extended X-ray absorption fine structure of tungsten. *Model. Simul. Mater. Sci. Eng.*, *26*, 025004. doi:`10.1088/1361-651X/aa9bab`.

Keen, D., & McGreevy, R. (1990). Structural modelling of glasses using reverse Monte Carlo simulation. *Nature*, *344*, 423–425. doi:`10.1038/344423a0`.

Keski-Rahkonen, O., & Krause, M. O. (1974). Total and partial atomic-level widths. *Atomic Data and Nuclear Data Tables*, *14*, 139–146. doi:`10.1016/S0092-640X(74)80020-3`.

Kim, M., Oh, I., Choi, H., Jang, W., Song, J., Kim, C. S., Yoo, J.-W., & Cho, S. (2022). A solution-based route to compositionally complex metal oxide structures using high-entropy layered double hydroxides. *Cell Rep. Phys. Sci.*, *3*, 100702. doi:`10.1016/j.xcrp.2021.100702`.

Krayzman, V., & Levin, I. (2010). Reverse Monte Carlo refinements of local displacive order in perovskites: $AgNbO_3$ case study. *J. Phys.: Condens. Matter*, *22*, 404201. doi:`10.1088/0953-8984/22/40/404201`.

Krayzman, V., Levin, I., Woicik, J. C., Proffen, T., Vanderah, T. A., & Tucker, M. G. (2009). A combined fit of total scattering and extended X-ray absorption fine structure data for local-structure determination in crystalline materials. *J. Appl. Crystallogr.*, *42*, 867–877. doi:`10.1107/S0021889809023541`.

Kuzmin, A., Anspoks, A., Kalinko, A., & Timoshenko, J. (2016). The use of X-ray absorption spectra for validation of classical force-field models. *Z. Phys. Chem.*, *230*, 537–549. doi:`10.1515/zpch-2015-0664`.

Kuzmin, A., & Chaboy, J. (2014). EXAFS and XANES analysis of oxides at the nanoscale. *IUCrJ*, *1*, 571–589. doi:`10.1107/S205225251402110`.

Kuzmin, A., & Evarestov, R. A. (2009). Quantum mechanics-molecular dynamics approach to the interpretation of X-ray absorption spectra. *J. Phys.: Condens. Matter*, *21*, 055401. doi:`10.1088/0953-8984/21/5/055401`.

Kuzmin, A., & Purans, J. (1993). The influence of the focusing effect on the X-ray absorption fine structure above all the tungsten L edges in non-stoichiometric tungsten oxides. *J. Phys.: Condens. Matter*, *5*, 9423–9430. doi:`10.1088/0953-8984/5/50/023`.

Kuzmin, A., Timoshenko, J., Kalinko, A., Jonane, I., & Anspoks, A. (2020). Treatment of disorder effects in X-ray absorption spectra beyond the conventional approach. *Radiation Physics and Chemistry*, *175*, 108112. doi:`10.1016/j.radphyschem.2018.12.032`.

Lee, P. A., Citrin, P. H., Eisenberger, P., & Kincaid, B. M. (1981). Extended X-ray absorption fine structure - its strengths and limitations as a structural tool. *Rev. Mod. Phys.*, *53*, 769–806. doi:`10.1103/RevModPhys.53.769`.

Lee, P. A., & Pendry, J. B. (1975). Theory of the extended X-ray absorption fine structure. *Phys. Rev. B*, *11*, 2795–2811. doi:`10.1103/PhysRevB.11.2795`.

Leetmaa, M., Wikfeldt, K. T., & Pettersson, L. G. M. (2010). SpecSwap-RMC: a novel reverse Monte Carlo approach using a discrete set of local configurations and pre-computed properties. *J. Phys.: Condens. Matter*, *22*, 135001. doi:`10.1088/0953-8984/22/13/135001`.

Lei, Z., Liu, X., Wang, H., Wu, Y., Jiang, S., & Lu, Z. (2019). Development of advanced materials via entropy engineering. *Scr. Mater.*, *165*, 164–169. doi:`10.1016/j.scriptamat.2019.02.015`.

Levin, I., Krayzman, V., & Woicik, J. C. (2014). Local structure in perovskite BaSrTiO$_3$: Reverse Monte Carlo refinements from multiple measurement techniques. *Phys. Rev. B*, *89*, 024106. doi:`10.1103/PhysRevB.89.024106`.

Liu, X., Zhang, J., & Pei, Z. (2023). Machine learning for high-entropy alloys: Progress, challenges and opportunities. *Prog. Mater. Sci.*, *131*, 101018. doi:`10.1016/j.pmatsci.2022.101018`.

Luo, X.-F., Patra, J., Chuang, W.-T., Nguyen, T. X., Ting, J.-M., Li, J., Pao, C.-W., & Chang, J.-K. (2022). Charge–discharge mechanism of high-entropy Co-free spinel oxide to-ward Li^+ storage examined using operando quick-scanning X-ray absorption spectroscopy. *Adv. Sci.*, *9*, 2201219. doi:`10.1002/advs.202201219`.

Ma, Y., Ma, Y., Dreyer, S. L., Wang, Q., Wang, K., Goonetilleke, D., Omar, A., Mikhailova, D., Hahn, H., Breitung, B., & Brezesinski, T. (2021). High-entropy metal-organic frameworks for highly reversible sodium storage. *Adv. Mater.*, *33*, 2101342. doi:`10.1002/adma.202101342`.

Markland, T., & Ceriotti, M. (2018). Nuclear quantum effects enter the mainstream. *Nat. Rev. Chem.*, *2*, 0109. doi:`10.1038/s41570-017-0109`.

Marx, D., & Parrinello, M. (1996). Ab initio path integral molecular dynamics: basic ideas. *J. Chem. Phys.*, *104*, 4077. doi:`10.1063/1.471221`.

Maulik, O., Patra, N., Bhattacharyya, D., Jha, S., & Kumar, V. (2017). Local atomic structure investigation of $AlFeCuCrMg_x$ (0.5, 1, 1.7) high entropy alloys: X-ray absorption spectroscopy study. *Solid State Commun.*, *252*, 73–77. doi:`10.1016/j.ssc.2017.01.018`.

McGreevy, R. L. (2001). Reverse Monte Carlo modelling. *J. Phys.: Condens. Matter*, *13*, R877–R913. doi:`10.1088/0953-8984/13/46/201`.

McGreevy, R. L., & Pusztai, L. (1988). Reverse Monte Carlo simulation: A new technique for the determination of disordered structures. *Mol. Simul.*, *1*, 359–367. doi:`10.1080/08927028808080958`.

Merkling, P. J., Muñoz Páez, A., Pappalardo, R. R., & Sánchez Marcos, E. (2001). Combination of XANES spectroscopy and molecular dynamics to probe the local structure in disordered systems. *Phys. Rev. B*, *64*, 092201. doi:`10.1103/PhysRevB.64.092201`.

Metropolis, N., Rosenbluth, A. W., Rosenbluth, M. N., Teller, A. H., & Teller, E. (1953). Equation of state calculations by fast computing machines. *J. Chem. Phys.*, *21*, 1087–1092. doi:`10.1063/1.1699114`.

Miracle, D., & Senkov, O. (2017). A critical review of high entropy alloys and related concepts. *Acta Mater.*, *122*, 448–511. doi:`10.1016/j.actamat.2016.08.081`.

Molenda, J., Milewska, A., Zając, W., Walczak, K., Wolczko, M., Komenda, A., & Tobola, J. (2023). Impact of O3/P3 phase transition on the performance of the $Na_xTi_{1/6}Mn_{1/6}Fe1/6Co_{1/6}Ni_{1/6}Cu_{1/6}O_2$ cathode material for Na-ion batteries. *J. Mater. Chem. A*, *11*, 4248–4260. doi:`10.1039/D2TA08431G`.

Morris, D., Yao, Y., Finfrock, Y. Z., Huang, Z., Shahbazian-Yassar, R., Hu, L., & Zhang, P. (2021). Composition-dependent structure and properties of 5- and 15-element high-entropy alloy nanoparticles. *Cell Rep. Phys. Sci.*, *2*, 100641. doi:`10.1016/j.xcrp.2021.100641`.

Müller, J., Jepsen, O., & Wilkins, J. (1982). X-ray absorption spectra: K-edges of 3d transition metals, L-edges of 3d and 4d metals, and M-edges of palladium. *Solid State Communications*, *42*, 365–368. doi:`10.1016/0038-1098(82)90154-5`.

Muller, J. E., Jepsen, O., Andersen, O. K., & Wilkins, J. W. (1978). Systematic Structure in the K-Edge Photoabsorption Spectra of the 4d Transition Metals: Theory. *Phys. Rev. Lett.*, *40*, 720–722. doi:`10.1103/PhysRevLett.40.720`.

Natoli, C. R., Benfatto, M., Brouder, C., López, M. F. R., & Foulis, D. L. (1990). Multichannel multiple-scattering theory with general potentials. *Phys. Rev. B*, *42*, 1944–1968. doi:`10.1103/PhysRevB.42.1944`.

Nemani, S., Torkamanzadeh, M., Wyatt, B., Presser, V., & Anasori, B. (2023). Functional two-dimensional high-entropy materials. *Commun. Mater.*, *4*, 16. doi:`10.1038/s43246-023-00341-y`.

Okamoto, Y. (2004). XAFS simulation of highly disordered materials. *Nucl. Instrum. Methods Phys. Res. A*, *526*, 572–583. doi:`10.1016/j.nima.2004.02.025`.

Okamoto, Y., Akabori, M., Motohashi, H., Itoh, A., & Ogawa, T. (2002). High-temperature XAFS measurement of molten salt systems. *Nucl. Instrum. Meth. Phys. Res. A*, *487*, 605–611. doi:`10.1016/S0168-9002(01)02202-1`.

Pierce, L. C., Salomon-Ferrer, R., Augusto F. de Oliveira, C., McCammon, J. A., & Walker, R. C. (2012). Routine access to millisecond time scale events with accelerated molecular dynamics. *J. Chem. Theory Comput.*, *8*, 2997–3002. doi:`10.1021/ct300284c`.

Price, S. W. T., Zonias, N., Skylaris, C.-K., Hyde, T. I., Ravel, B., & Russell, A. E. (2012). Fitting EXAFS data using molecular dynamics outputs and a histogram approach. *Phys. Rev. B*, *85*, 075439. doi:`10.1103/PhysRevB.85.075439`.

Pugliese, G., Tortora, L., Tomassucci, G., Kasem, R., Mizokawa, T., Mizuguchi, Y., & Saini, N. (2023). Possible local order in the high entropy $TrZr_2$ superconductors. *J. Phys. Chem. Solids*, *174*, 111154. doi:`10.1016/j.jpcs.2022.111154`.

Qi, B., Perez, I., Ansari, P. H., Lu, F., & Croft, M. (1987). L_2 and L_3 measurements of transition-metal 5d orbital occupancy, spin-orbit effects, and chemical bonding. *Phys. Rev. B*, *36*, 2972–2975. doi:`10.1103/PhysRevB.36.2972`.

Qian, X., Han, D., Zheng, L., Chen, J., Tyagi, M., Li, Q., Du, F., Zheng, S., Huang, X., Zhang, S., Shi, J., Huang, H., Shi, X., Chen, J., Qin, H., Bernholc, J., Chen, X., Chen, L.-Q., Hong, L., & Zhang, Q. M. (2021). High-entropy polymer produces a giant electrocaloric effect at low fields. *Nature*, *600*, 664–669. doi:`10.1038/s41586-021-04189-5`.

Rehr, J. J., & Albers, R. C. (2000). Theoretical approaches to X-ray absorption fine structure. *Rev. Mod. Phys.*, *72*, 621–654. doi:`10.1103/RevModPhys.72.621`.

Rehr, J. J., Kas, J. J., Prange, M. P., Sorini, A. P., Takimoto, Y., & Vila, F. (2009). Ab initio theory and calculations of X-ray spectra. *C. R. Phys.*, *10*, 548–559. doi:`10.1016/j.crhy.2008.08.004`.

Rehr, J. J., Kas, J. J., Vila, F. D., Prange, M. P., & Jorissen, K. (2010). Parameter-free calculations of X-ray spectra with FEFF9. *Phys. Chem. Chem. Phys.*, *12*, 5503–5513. doi:`10.1039/B926434E`.

Ritter, T. G., Phakatkar, A. H., Rasul, M. G., Saray, M. T., Sorokina, L. V., Shokuhfar, T., Gonçalves, J. M., & Shahbazian-Yassar, R. (2022). Electrochemical synthesis of high entropy hydroxides and oxides boosted by hydrogen evolution reaction. *Cell Rep. Phys. Sci.*, *3*, 100847. doi:`10.1016/j.xcrp.2022.100847`.

Rost, C. M., Sachet, E., Borman, T., Moballegh, A., Dickey, E. C., Hou, D., Jones, J. L., Curtarolo, S., & Maria, J.-P. (2015). Entropy-stabilized oxides. *Nat. Commun.*, *6*, 8485. doi:`10.1038/ncomms9485`.

Ruiz-Lopez, M., Loos, M., Goulon, J., Benfatto, M., & Natoli, C. (1988). Reinvestigation of the EXAFS and XANES spectra of ferrocene and nickelocene in the framework of the multiple scattering theory. *Chem. Phys.*, *121*, 419–437. doi:`10.1016/0301-0104(88)87246-X`.

Sapelkin, A. V., & Bayliss, S. C. (2002). Distance dependence of mean-square relative displacements in EXAFS. *Phys. Rev. B*, *65*, 172104. doi:`10.1103/PhysRevB.65.172104`.

Sarkar, A., Velasco, L., Wang, D., Wang, Q., Talasila, G., de Biasi, L., Kübel, C., Brezesinski, T., Bhattacharya, S. S., Hahn, H., & Breitung, B. (2018). High entropy oxides for reversible energy storage. *Nat. Commun.*, *9*, 3400. doi:`10.1038/s41467-018-05774-5`.

Sayers, D. E., Stern, E. A., & Lytle, F. W. (1971). New technique for investigating noncrystalline structures: Fourier analysis of the extended X-ray-absorption fine structure. *Phys. Rev. Lett.*, *27*, 1204–1207. doi:`10.1103/PhysRevLett.27.1204`.

Shapeev, A. V., Bocharov, D., & Kuzmin, A. (2022). Validation of moment tensor potentials for fcc and bcc metals using EXAFS spectra. *Comput. Mater. Sci.*, *210*, 111028. doi:`10.1016/j.commatsci.2021.111028`.

Smekhova, A., Kuzmin, A., Siemensmeyer, K., Abrudan, R., Reinholz, U., Buzanich, A. G., Schneider, M., Laplanche, G., & Yusenko, K. V. (2022a). Inner relaxations in equiatomic single-phase high-entropy cantor alloy. *J. Alloys Compd.*, *920*, 165999. doi:`10.1016/j.jallcom.2022.165999`.

Smekhova, A., Kuzmin, A., Siemensmeyer, K., Luo, C., Chen, K., Radu, F., Weschke, E., Reinholz, U., Buzanich, A. G., & Yusenko, K. V. (2022b). Al-driven peculiarities of local coordination and magnetic properties in single-phase Al_x-CrFeCoNi high-entropy alloys. *Nano Res.*, *15*, 4845–4858. doi:`10.1007/s12274-021-3704-5`.

Smekhova, A., Kuzmin, A., Siemensmeyer, K., Luo, C., Taylor, J., Thakur, S., Radu, F., Weschke, E., Buzanich, A. G., Xiao, B., Savan, A., Yusenko, K. V., & Ludwig, A. (2023).

Local structure and magnetic properties of a nanocrystalline Mn-rich Cantor alloy thin film down to the atomic scale. *Nano Res.*, *16*, 5626–5639. doi:`10.1007/s12274-022-5135-3`.

Sun, X., Sun, F., Sun, Z., Chen, J., Du, X., Wang, J., Jiang, Z., & Huang, Y. (2017). Disorder effects on EXAFS modeling for catalysts working at elevated temperatures. *Rad. Phys. Chem.*, *137*, 93–98. doi:`10.1016/j.radphyschem.2016.01.039`.

Sushil, J., Kumar, A., Gautam, A., & Ahmad, M. I. (2021). High entropy phase evolution and fine structure of five component oxide (Mg, Co, Ni, Cu, Zn)O by citrate gel method. *Mater. Chem. Phys.*, *259*, 124014. doi:`10.1016/j.matchemphys.2020.124014`.

Tamm, A., Aabloo, A., Klintenberg, M., Stocks, M., & Caro, A. (2015). Atomic-scale properties of Ni-based FCC ternary, and quaternary alloys. *Acta Mater.*, *99*, 307–312. doi:`10.1016/j.actamat.2015.08.015`.

Tan, Y.-Y., Li, T., Chen, Y., Chen, Z.-J., Su, M.-Y., Zhang, J., Gong, Y., Wu, T., Wang, H.-Y., & Dai, L.-H. (2023). Uncovering heterogeneity of local lattice distortion in TiZrHfNbTa refractory high entropy alloy by SR-XRD and EXAFS. *Scr. Mater.*, *223*, 115079. doi:`10.1016/j.scriptamat.2022.115079`.

Tan, Y.-Y., Su, M.-Y., Xie, Z.-C., Chen, Z.-J., Gong, Y., Zheng, L.-R., Shi, Z., Mo, G., Li, Y., Li, L.-W., Wang, H.-Y., & Dai, L.-H. (2021). Chemical composition dependent local lattice distortions and magnetism in high entropy alloys. *Intermetallics*, *129*, 107050. doi:`10.1016/j.intermet.2020.107050`.

Tavani, F., Fracchia, M., Pianta, N., Ghigna, P., Quartarone, E., & D'Angelo, P. (2020). Multivariate curve resolution analysis of operando XAS data for the investigation of the lithiation mechanisms in high entropy oxides. *Chem. Phys. Lett.*, *760*, 137968. doi:`10.1016/j.cplett.2020.137968`.

Tavani, F., Fracchia, M., Tofoni, A., Braglia, L., Jouve, A., Morandi, S., Manzoli, M., Torelli, P., Ghigna, P., & D'Angelo, P. (2021). Structural and mechanistic insights into low-temperature CO oxidation over a prototypical high entropy oxide by Cu L-edge operando soft X-ray absorption spectroscopy. *Phys. Chem. Chem. Phys.*, *23*, 26575–26584. doi:`10.1039/D1CP03946F`.

Teo, B. K. (1986). *EXAFS: Basic Principles and Data Analysis*. Berlin: Springer.

Teplonogova, M., Yapryntsev, A., Baranchikov, A., & Ivanov, V. (2022). High-entropy layered rare earth hydroxides. *Inorg. Chem.*, *61*, 19817–19827. doi:`10.1021/acs.inorgchem.2c02950`.

Timoshenko, J., Anspoks, A., Kalinko, A., & Kuzmin, A. (2014a). Analysis of extended X-ray absorption fine structure data from copper tungstate by the reverse Monte Carlo method. *Phys. Scr.*, *89*, 044006. doi:`10.1088/0031-8949/89/04/044006`.

Timoshenko, J., Anspoks, A., Kalinko, A., & Kuzmin, A. (2014b). Temperature dependence of the local structure and lattice dynamics of wurtzite-type ZnO. *Acta Mater.*, *79*, 194–202. doi:`10.1016/j.actamat.2014.07.029`.

Timoshenko, J., & Kuzmin, A. (2009). Wavelet data analysis of EXAFS spectra. *Comput. Phys. Commun.*, *180*, 920–925. doi:`10.1016/j.cpc.2008.12.020`.

Timoshenko, J., Kuzmin, A., & Purans, J. (2012). Reverse Monte Carlo modeling of thermal disorder in crystalline materials from EXAFS spectra. *Comput. Phys. Commun.*, *183*, 1237–1245. doi:`10.1016/j.cpc.2012.02.002`.

Timoshenko, J., Kuzmin, A., & Purans, J. (2014c). EXAFS study of hydrogen intercalation into ReO_3 using the evolutionary algorithm. *J. Phys.: Condens. Matter*, *26*, 055401. doi:`10.1088/0953-8984/26/5/055401`.

Timoshenko, J., Lu, D., Lin, Y., & Frenkel, A. I. (2017). Supervised machine-learning-based determination of three-dimensional structure of metallic nanoparticles. *J. Phys. Chem. Lett.*, *8*, 5091–5098. doi:`10.1021/acs.jpclett.7b02364`.

Tranquada, J. M., & Ingalls, R. (1983). Extended x-ray-absorption fine-structure study of anharmonicity in CuBr. *Phys. Rev. B*, *28*, 3520–3528. doi:`10.1103/PhysRevB.28.3520`.

Tucker, M. G., Keen, D. A., Dove, M. T., Goodwin, A. L., & Hui, Q. (2007). RMCProfile: reverse Monte Carlo for polycrystalline materials. *J. Phys.: Condens. Matter*, *19*, 335218. doi:`10.1088/0953-8984/19/33/335218`.

Tuckerman, M. E., Ungar, P. J., von Rosenvinge, T., & Klein, M. L. (1996). Ab initio molecular dynamics simulations. *J. Phys. Chem.*, *100*, 12878–12887. doi:`10.1021/jp960480+`.

Walczak, K., Plewa, A., Ghica, C., Zając, W., Trenczek-Zając, A., Zając, M., Toboła, J., & Molenda, J. (2022). $NaMn_{0.2}Fe_{0.2}Co_{0.2}Ni_{0.2}Ti_{0.2}O_2$ high-entropy layered oxide – experimental and theoretical evidence of high electrochemical performance in sodium batteries. *Energy Storage Mater.*, *47*, 500–514. doi:`10.1016/j.ensm.2022.02.038`.

Wang, J., Dreyer, S. L., Wang, K., Ding, Z., Diemant, T., Karkera, G., Ma, Y., Sarkar, A., Zhou, B., Gorbunov, M. V., Omar, A., Mikhailova, D., Presser, V., Fichtner, M., Hahn, H., Brezesinski, T., Breitung, B., & Wang, Q. (2022). P2-type layered high-entropy oxides as sodium-ion cathode materials. *Mater. Futures*, *1*, 035104. doi:`10.1088/2752-5724/ac8ab9`.

Wang, K., Hua, W., Huang, X., Stenzel, D., Wang, J., Ding, Z., Cui, Y., Wang, Q., Ehrenberg, H., Breitung, B., Kübel, C., & Mu, X. (2023). Synergy of cations in high entropy oxide lithium ion battery anode. *Nat. Commun.*, *14*, 1487. doi:`10.1038/s41467-023-37034-6`.

Wei, P.-C., Liao, C.-N., Wu, H.-J., Yang, D., He, J., Biesold-McGee, G. V., Liang, S., Yen, W.-T., Tang, X., Yeh, J.-W., Lin, Z., & He, J.-H. (2020). Thermodynamic routes to ultralow thermal conductivity and high thermoelectric performance. *Adv. Mater.*, *32*, 1906457. doi:`10.1002/adma.201906457`.

Winterer, M. (2000). Reverse Monte Carlo analysis of extended X-ray absorption fine structure spectra of monoclinic and amorphous zirconia. *J. Appl. Phys.*, *88*, 5635–5644. doi:`10.1063/1.1319167`.

Woicik, J. C., Cockayne, E., Shirley, E. L., Levin, I., Weiland, C., Ravel, B., & Abeykoon, A. M. M. (2023). Lattice vibrations and energy landscape of the isoelectronic semiconductor series CuBr, ZnSe, GaAs, and Ge: The special case of CuBr and its *d*-level chemistry. *Phys. Rev. B*, *108*, 195202. doi:`10.1103/PhysRevB.108.195202`.

Wu, T., Chen, Y., Shi, S., Wu, M., Gui, W., Tan, Y., Li, J., & Wu, Y. (2021). Effects of W alloying on the lattice distortion and wear behavior of laser cladding AlCoCrFeNiW$_x$ high-entropy alloy coatings. *Materials*, *14*, 5450. doi:`10.3390/ma14185450`.

Xiang, H., Xing, Y., Dai, F., Wang, H., Su, L., Miao, L., Zhang, G., Wang, Y., Qi, X., Yao, L., Wang, H., Zhao, B., Li, J., & Zhou, Y. (2021). High-entropy ceramics: Present status, challenges, and a look forward. *J. Adv. Ceram.*, *10*, 385–441. doi:`10.1007/s40145-021-0477-y`.

Xu, H., Zhang, Z., Liu, J., Do-Thanh, C.-L., Chen, H., Xu, S., Lin, Q., Jiao, Y., Wang, J., Wang, Y., Chen, Y., & Dai, S. (2020). Entropy-stabilized single-atom Pd catalysts via high-entropy fluorite oxide supports. *Nat. Commun.*, *11*, 3908. doi:`10.1038/s41467-020-17738-9`.

Yancey, D. F., Chill, S. T., Zhang, L., Frenkel, A. I., Henkelman, G., & Crooks, R. M. (2013). A theoretical and experimental examination of systematic ligand-induced disorder in Au dendrimer-encapsulated nanoparticles. *Chem. Sci.*, *4*, 2912–2921. doi:`10.1039/C3SC50614B`.

Yang, Y., & Kawazoe, Y. (2012). Characterization of zero-point vibration in one-component crystals. *EPL*, *98*, 66007. doi:`10.1209/0295-5075/98/66007`.

Yeh, J.-W., Chen, S.-K., Lin, S.-J., Gan, J.-Y., Chin, T.-S., Shun, T.-T., Tsau, C.-H., & Chang, S.-Y. (2004). Nanostructured high-entropy alloys with multiple principal elements: novel alloy design concepts and outcomes. *Adv. Eng. Mater.*, *6*, 299–303. doi:`10.1002/adem.200300567`.

Yuan, S., Qin, J.-S., Li, J., Huang, L., Feng, L., Fang, Y., Lollar, C., Pang, J., Zhang, L., Sun, D., Alsalme, A., Cagin, T., & Zhou, H.-C. (2022). Retrosynthesis of multi-component metal-organic frameworks. *Nat. Commun.*, *9*, 808. doi:`10.1038/s41467-018-03102-5`.

Zhang, F., & Song, H.-Q. (2022). Effect of atomic size mismatch and chemical complexity on the local lattice distortion of BCC solid solution alloys. *Mater. Today Commun.*, *33*, 104367. doi:`10.1016/j.mtcomm.2022.104367`.

Zhang, F., Tong, Y., Jin, K., Bei, H., Weber, W. J., Huq, A., Lanzirotti, A., Newville, M., Pagan, D. C., Ko, J. Y. P., & Zhang, Y. (2018). Chemical complexity induced local structural distortion in NiCoFeMnCr high-entropy alloy. *Mater. Res. Lett.*, *6*, 450–455. doi:`10.1080/21663831.2018.1478332`.

Zhang, F. X., Zhao, S., Jin, K., Xue, H., Velisa, G., Bei, H., Huang, R., Ko, J. Y. P., Pagan, D. C., Neuefeind, J. C., Weber, W. J., & Zhang, Y. (2017). Local structure and short-range order in a NiCoCr solid solution alloy. *Phys. Rev. Lett.*, *118*, 205501. doi:`10.1103/PhysRevLett.118.205501`.

Zhang, X., Luan, H., Lou, H., Liang, T., Chen, S., Xu, D., Yin, Z., Wang, L., Zeng, J., Ren, Y., Zeng, Z., Shao, Y., Yao, K.-F., & Zeng, Q. (2022a). Highly variable chemical short-range order in a high-entropy metallic glass. *Mater. Today Phys.*, *27*, 100799. doi:`10.1016/j.mtphys.2022.100799`.

Zhang, Y., Eremenko, M., Krayzman, V., Tucker, M. G., & Levin, I. (2020). New capabilities for enhancement of RMCProfile: instrumental profiles with arbitrary peak shapes for structural refinements using the reverse Monte Carlo method. *Journal of Applied Crystallography*, *53*, 1509–1518. doi:`10.1107/S1600576720013254`.

Zhang, Y., Osetsky, Y. N., & Weber, W. J. (2022b). Tunable chemical disorder in concentrated alloys: defect physics and radiation performance. *Chem. Rev.*, *122*, 789–829. doi:`10.1021/acs.chemrev.1c00387`.

the Institute of Solid State Physics, University of Latvia, as a centre of excellence, has received funding from the European Union's Horizon 2020 Framework Programme H2020-WIDESPREAD-01-2016-2017-TeamingPhase2 under grant agreement no. 739508, project CAMART2.